Age and composition of the youngest basalts on the Moon returned by the Chang'e-5

Document Version
Accepted author manuscript

[Link to publication record in Manchester Research Explorer](#)

Citing this paper
Please note that where the full-text provided on Manchester Research Explorer is the Author Accepted Manuscript or Proof version this may differ from the final Published version. If citing, it is advised that you check and use the publisher's definitive version.

OPEN ACCESS

Title: Age and composition of the youngest basalts on the Moon returned by the Chang'e-5

Authors: Xiaochao Che[1], Alexander Nemchin[2,1]*, Dunyi Liu[1,3]*, Tao Long[1], Chen Wang[1], Marc D. Norman[4], Katherine H. Joy[5], Romain Tartese[5], James Head[6], Bradley Jolliff[7], Joshua F. Snape[5], Clive R. Neal[8], Martin J. Whitehouse[9], Carolyn Crow[10], Gretchen Benedix[2], Fred Jourdan[2], Zhiqing Yang[1], Chun Yang[1], Jianhui Liu[1], Shiwen Xie[1], Zemin Bao[1], Runlong Fan[1], Dapeng Li[3], Zengsheng Li[3], Stuart G. Webb[8]

Affiliations:

[1]Beijing SHRIMP (Sensitive High Resolution Ion Micro Probe) Center, Institute of Geology, Chinese Academy of Geological Sciences, Beijing 100037, China

[2]School of Earth and Planetary Sciences, Curtin University, Perth, WA 6845, Australia

[3]Shandong Institute of Geological Sciences, Jinan, Shandong 250013, China

[4]Research School of Earth Sciences, The Australian National University, Canberra ACT 2601 Australia.

[5]Department of Earth and Environmental Sciences, The University of Manchester, Manchester, M13 9PL, UK.

[6]Department of Earth, Environmental, and Planetary Sciences, Brown University, Providence 02912, USA

[7]Department of Earth and Planetary Sciences and The McDonnell Center for the Space Sciences, Washington University in St. Louis, St. Louis, MO 63130, USA

^{8}Department of Civil and Environmental Engineering and Earth Sciences, University of Notre Dame, Notre Dame, IN 46556, USA

^{9}Department of Geosciences, Swedish Museum of Natural History, SE-104 05 Stockholm, Sweden.

^{10}Department of Geological Sciences, University of Colorado Boulder 80309, USA

*Corresponding authors: liudunyi@bjshrimp.cn

a.nemchin@curtin.edu.au

Abstract: The youngest volcanic units on the Moon are basalt lavas in Oceanus Procellarum, a region with high levels of the heat-producing elements potassium, thorium, and uranium. The Chang'e-5 mission sampled these young lunar basalts and returned them for laboratory analysis. Here we report an age of 1963±57 Ma and the chemical and mineralogical compositions of these lavas. This age constrains the lunar impact chronology of the inner solar system and the thermal evolution of the Moon. High concentrations of heat-producing elements in the deep mantle of the Moon are not required to generate these lavas so alternate explanations are needed to account for the longevity of lunar magmatism.

Main Text:

The Oceanus Procellarum region of the Moon is uniquely characterized by high concentrations of potassium, thorium, and uranium, elements that generate heat through long-lived radioactive decay and may have sustained prolonged magmatic activity on the near side of the Moon. The Chang'e-

5 spacecraft landed in this region at 43.06°N, 51.92°W, about 170 km ENE of Mons Rümker, with the aim of sampling the youngest basalt lavas on the Moon. Orbital data have shown that the geologic unit (designated Em4/P58) exposed around the landing site has high levels of Th (5-8.5 ppm), intermediate to high Ti abundances (5-8% TiO_2), and relatively high concentrations of the minerals clinopyroxene and olivine (about 31 and 13%, respectively) *(1-3)*. The mission goal was to return samples of young lunar basalts that were identified based on the spatial density of impact craters *(1,4)* in order to address outstanding problems of planetary evolution.

The number of impact craters on a surface reflects its relative age, with older surfaces having more craters. The Moon is the only planetary body where impact crater ages have been quantified, and the lunar chronology is used to calibrate the ages of other planetary surfaces throughout the Solar System. For example, the climatic evolution of Mars is related directly to the lunar cratering chronology, but the chronology is highly uncertain for ages younger than ~3 Ga *(5)*.

Young volcanism on a small body such as the Moon also poses a challenge for understanding its thermal evolution. Although the young basaltic eruptions on the Moon clearly occurred in regions of elevated heat-producing elements such as K, Th, and U, the significance of this association for melting deep within the Moon is not clear *(6,7)*.

Here, we present mineralogical, chemical and U-Th-Pb isotopic characteristics of two basalt fragments collected by the Chang'e-5 mission. Our goal is to constrain the wide range of impact crater ages predicted for the Em4/P58 basaltic unit at the landing site, which vary from 1.2 to 3.2 Ga *(1,3, 8-14)*. We also present compositions of these basalts to assess their magmatic source and petrogenesis, and to provide calibration for estimates of lunar surface compositions based on remote observations *(15)*.

We obtained two fragments, referred to here as CE5-B1 and CE5-B2 *(16)*. Both are equidimensional, approximately 3-4 mm in size and consist of minerals common in lunar basalts, such as chemically zoned clinopyroxene, plagioclase, olivine, and ilmenite, with small amounts of quartz and cristobalite (Fig. 1; Data S1, see also supplementary text). Both contain multiple

70 interstitial pockets of K-rich glass, barian K-feldspar, troilite, Ca-phosphates (apatite and merrillite), and the Zr-rich minerals baddeleyite and zirconolite. Metallic iron is absent. Both fragments have igneous textures that differ slightly in grain size and crystal habits: CE5-B1 is finer-grained (≤1 mm long) with radiating elongated crystals of plagioclase and ilmenite, whereas CE5-B2 is coarser-grained (<2 mm long) (Fig. 1, see also supplementary text). These textures

75 indicate crystallization from a molten magma (melt) and that CE5-B1 cooled more rapidly than CE5-B2. Most mineral phases in CE5-B2 are highly fractured, and shock-melt pockets and veins (a few tens of microns wide) are present along one edge of the sample (lower right portion of Fig. 1). In contrast, CE5-B1 has no obvious shock-melt pockets or veins and displays fewer fractures ~1-10 microns in width. Raman analysis of major and some accessory minerals in both fragments

80 (see supplementary text) indicates that shock-induced maskelynite is present only in the shock melt zone of fragment CE5-B2. All other minerals (including plagioclase) outside of this zone have not been modified by shock and preserve their primary magmatic crystallinity (see supplementary text).

The pyroxenes and olivines in the two fragments vary widely in their Mg/Fe ratio and include

85 some of the most Fe-rich compositions measured in lunar basalts (Data S1). The mineral chemistries of these two fragments differ slightly and appear to correspond to their textures (Data S1). For example, the olivine in CE5-B2 is more Fe-rich whereas CE5-B1 has a wider range of TiO_2, Al_2O_3, and Cr_2O_3 in pyroxene (Data S1). The mineralogy of these fragments is similar to that of other known lunar basalts. The K-rich glass and the presence of Zr-bearing minerals raise

90   the possibility of a mantle component enriched in heat-producing elements, but these basalts

appear to be compositionally fractionated, so the presence of these evolved minerals may instead

reflect a small degree of partial melting and/or extensive fractional crystallization.

The bulk compositions of both fragments calculated from their modal mineralogy indicate elevated

FeO (~22-25 wt.%) and low MgO (~5 wt.%). Their TiO_2 contents (~6-8 wt.%) Al_2O_3, (<11 wt.%),

95   and K concentrations (<2000 ppm) are consistent with high-Ti, low-Al, low-K mare basalts in

standard classifications [17] (Table S1; Fig. 2). The mineralogy and bulk compositions of these

samples are consistent with remote sensing observations of this region, implying that they are

representative samples of the Em4 unit, despite the differences in grainsize and inferred cooling

history of CE5-B1 and CE5-B2. However, given the small size of these fragments it is possible

100   that these calculated bulk compositions are not fully representative of the melts from which they

formed, especially for the coarser-grained fragment CE5-B2.

The Pb isotope ratios of the two fragments were analyzed in 50 selected locations (spots of about

7 μm in diameter) within phosphate grains, barian K-feldspar grains, K-rich glass pockets, and

areas containing Zr-rich minerals (Fig. 3, Data S4). Determining U-Th-Pb ages of lunar basalts

105   requires knowledge of their initial Pb composition. We adopt an isochron approach in which the

data are presented in $^{207}Pb/^{206}Pb$ vs. $^{204}Pb/^{206}Pb$ coordinates. This method allows both the age and

the initial Pb isotopic composition to be obtained and has been demonstrated through the Pb-Pb

study of multiple Apollo basalts [16, 18]. The ubiquitous presence of terrestrial contamination in

all lunar samples complicates interpretation of the data but is also accounted for in the isochron

110   approach. The individual isochron ages obtained for fragments CE5-B1 and CE5-B2 are 1893±280

Ma and 1966±59 Ma, respectively. Combining all data for the two fragments, which are consistent

within uncertainties, gives an age of 1963±57 Ma (Fig. 3a). Our estimate of the initial lunar Pb

isotopic composition ($^{204}Pb/^{206}Pb = 0.00226\pm0.00006$, $^{207}Pb/^{206}Pb = 0.815\pm0.009$ and $^{208}Pb/^{206}Pb$ = 0.926±0.013) is provided by the intercept of the isochron and the line fitted through four K-feldspar analyses (Fig. 3a).

Although the basalt fragments investigated here could be susceptible to partial resetting of the U-Pb system during impacts that transported the fragments to the Chang'e-5 landing site, or through subsequent Pb contamination from the host soil, we see no compelling evidence of this in the sample. Shock effects are apparent in one part of the sample CE5-B2, but no isotopic analyses were conducted in this part of the fragment (Fig. S6). Any secondary processes that mobilized Pb would also cause excess scatter in the isochron (i.e., specific minerals offset from the isochron by more than expected from the analytical uncertainties). Glass is most prone to Pb exchange, whereas Zr-rich minerals are likely to better preserve their original Pb isotope compositions even if shocked *(19)*. Shock-induced scatter would also be indicated by a large decrease of $^{207}Pb/^{206}Pb$ in less resistant phases; instead, we find the opposite trend in the $^{207}Pb/^{206}Pb$ vs. $^{204}Pb/^{206}Pb$ relationships (Fig.3). The best fit isochron constrained using only Zr-rich minerals indicates an age of 2011±50 Ma, consistent with the full dataset (Fig.3b). The spatially limited distribution of shock effects and intensity in different parts of the fragments, combined with the internal Pb isotope systematics of the samples, indicate that our measurements closely reflect the primary magmatic compositions of these samples.

Mineral and chemical characteristics of the two basalt fragments are consistent with those inferred for the Em4 unit identified at the landing site using remote sensing data *(1,2)*. Our isochron age is, therefore, representative of the emplacement age of Em4/P58 unit and has implications for lunar cratering chronology. Current model ages of the Em4 unit based on crater density measurements range widely from 1.21 Ga *(10)* to 3.3 Ga *(1)*, with the results of 1.91 Ga [Model A of (*3*)] and 2.07 Ga *(13)* being closest to our measured Pb-Pb crystallization age of 1.96-2.01 Ga. If this 1.96-

2.01 Ga age is representative of the Em4 unit, it implies that nearly 2000 km^3 of basaltic magma *(1)* erupted near the landing site almost 1 billion years later than the emplacement of any measured lunar basalts in the Apollo, Luna, and lunar meteorite sample collections *(18)*.

Chemical compositions of the two fragments analyzed here are distinct from those of lunar basalts from all other landing sites (Fig. 2). The Chang'e-5 basaltic fragments are more enriched in Fe and depleted in Mg than other sampled lunar basalts, which implies either an Fe-rich mantle source or unusual conditions of emplacement that allowed a greater extent of fractional crystallization of the magmas sampled by Chang'e-5. Extreme fractionation of the basaltic magmas may have contributed to the high Th concentrations measured remotely at the landing site (5-9 ppm). Alternatively, the high Th concentrations inferred from the remote sensing data may reflect either impact ejecta from the surrounding Oceanus Procellarum region or a primary magmatic component in the source of the Em4 basalts that links their petrogenesis to their spatial association with the high-Th region of the Oceanus Procellarum. The contribution of K-U-Th in the magmatic source or as a contaminant introduced during ascent and evolution of the magma can be assessed by the initial Pb isotopic composition as determined from the Pb-Pb isochrons. Assuming that the Pb-Pb system remained closed after the formation of these basalts and applying a single-stage Pb isotopic evolution model *(16)*, the source of the melt that formed the Chang'e-5 basalt fragments could have attained a Pb composition similar to that measured in the two fragments if the $^{238}U/^{204}Pb$ ratio of this source (referred to as the μ-value) was 665±3. This model does not consider possible fractionation of U and Pb during the earlier Lunar Magma Ocean (LMO) phase. For example, Apollo mare (formed within lunar maria) and KREEP (for high potassium, rare earth elements, and phosphorous) basalts have been used to constrain a multi-stage model of lunar Pb isotopic evolution that indicates a major differentiation event at 4.376 Ga *(20)*, possibly reflecting the final stages of LMO crystallization and formation of the source reservoir for KREEP, which is enriched

in all heat-producing elements *(20)*. Applying this multiple stage Pb isotope model to the Em4 basalts yields a slightly higher μ-value of 677±3.

These μ-values for the Em4 basalts imply only a modest (<1-2%) KREEP component either in their mantle sources or introduced by assimilation during magma ascent. This estimate shows that the Em4 basalts differ from the trend in source evolution previously suggested for Apollo samples, which show a progressive enrichment of their source regions in heat-producing elements as the basalts become younger *(18)*. If this enrichment trend extended to the Em4 basalts it would predict μ-values > 1000, which are not observed. Instead, the data suggest only a small amount of KREEP, at most, in these young basalts.

The emplacement age of 1963±57 Ma that we infer for the Em4 unit provides a calibration point for the lunar cratering (CSFD- crater size frequency distributions) chronology curve, which was previously unconstrained between ~1 and 3 Ga (Fig. 4) *(5, 21)*. This age for Em4 falls below many existing cratering chronology curves, indicating that the impact flux may have been lower than previously estimated at ages between the youngest Apollo-Luna basalts (~3.1 Ga) and that inferred for the Copernicus crater (~0.8 Ga), consistent with some chronology models *(22, 23)*. The number density of 1 km craters (N(1); Fig. 4) on the Em4 unit (1.24×10^{-3} to 1.74×10^{-3} km^{-2}) is similar to the upper limit measured for the Copernicus crater *(23, 24*; Fig. 4), so Copernicus might be older than the ~0.8 Ga radiometric age inferred from the ropy glasses sampled by Apollo 12 *(25)*.

The youngest basalts on the Moon lie within the Oceanus Procellarum, a region of the NW nearside characterized by thin crust and high concentrations of heat-producing elements such as K, Th, and U *(7)*. There is a strong spatial correlation between the occurrence of young lunar basalts and the concentrations of heat-producing elements *(26)* but the geophysical and geochemical basis for this correlation remains unclear. One possibility is that elevated radioactivity within the lunar

mantle produced long-lived thermal anomalies that enhance melting and generate young lunar
basalts *(7)*. This hypothesis predicts the young basalts carry elevated levels of heat-producing
elements, compared to the basalts that occur outside of the region enriched in these heat-producing
elements. Our Pb isotope results suggest that the Em4 unit and the source of its magma had U and
Th contents that were similar to those of Apollo and Luna mare basalts, suggesting that the mantle
source regions of the Em4 basalts did not have elevated contents of radioactive elements, and that
rising magmas were not mixed with KREEP during passage through the crust. Thus, alternative
explanations for the longevity of lunar magmatism such as tidal heating or a distinct source
mineralogy, supporting lower melting temperature of the mantle, are required. If so, this would
imply that the elevated Th content of the Em4 regolith recorded in remote sensing data could be
due to contamination by secondary ejecta from the Th-rich region of Oceanus Procellarum, which
occurs beneath and around the young basalt units *(1)*.

References

1. Y. Qian, et al., China's Chang'e-5 landing site: Geology, stratigraphy, and provenance of
    materials. *Earth Planet. Sci. Lett.* **561**, 116855 (2021). doi:10.1016/j.epsl.2021.116855

2. M. Lemelin, et al., The compositions of the lunar crust and upper mantle: Spectral analysis of
    the inner rings of lunar impact basins. *Planet. Space Sci*. 165, 230–243 (2019).
    doi:10.1016/j.pss.2018.10.003

3. T. Morota, et al., Timing and characteristics of the latest mare eruption on the Moon. *Earth
    Planet. Sci. Lett.* **302**, 255–266 (2011). doi:10.1016/j.epsl.2010.12.028

205   4. H. Hiesinger, J. W. Head, III, U. Wolf, R. Jaumann, G. Neukum, Ages and stratigraphy of

        mare basalts in Oceanus Procellarum, Mare Nubium, Mare Cognitum, and Mare Insularum.

        J. Geophys. Res. **108**, 5065 (2003). doi:10.1029/2002JE001985

    5. S. J. Robbins, New crater calibrations for the lunar crater-age chronology. *Earth Planet.*

        Sci. Lett. **403**, 188–198 (2014). doi:10.1016/j.epsl.2014.06.038

210   6. Snyder G.A, Borg L.E, Nyquist L.E, Taylor L.A, Chronology and isotopic constraints on

        lunar evolution in *Origin of the Earth and Moon* R. M. Canup, K. Righter K, eds.

        (University of Arizona Press, 2000), pp. 361–395.

    7. M. Laneuville, J. Taylor, M. A. Wieczorek, Distribution of Radioactive Heat Sources and

        Thermal History of the Moon. *J. Geophys. Res*. **123**, 3144–3166 (2018).

215   doi:10.1029/2018JE005742

    8. J. M. Boyce, Ages of flow units in the lunar nearside maria based on Lunar Orbiter IV

        photographs. *Proc. 7th Lunar Planet. Sci. Conf*. 2717-2728 (1976).

    9. H. Hiesinger, J. W. Head III, U. Wolf, R. Jaumann, G. Neukum, Ages and stratigraphy of

        lunar mare basalts: A synthesis. *Geol. Soc. Am. Special Papers* **477**, 1–51 (2011).

220   doi:10.1029/2009JE003380

    10. Y. Q. Qian, et al., Geology and Scientific Significance of the Rümker Region in Northern

        Oceanus Procellarum: China's Chang'E-5 Landing Region. *J. Geophys. Res*. **123**, 1407–

        1430 (2018). doi:10.1029/2018JE005595

    11. Y. Qian, et al., The regolith properties of the Chang'e-5 landing region and the ground

225   drilling experiments using lunar regolith simulants. *Icarus*. **337**, 113508 (2020).

        doi:10.1016/j.icarus.2019.113508

12. B. Wu, J. Huang, Y. Li, Y. Wang, J. Peng, Rock Abundance and Crater Density in the Candidate Chang'E-5 Landing Region on the Moon. *J. Geophys. Res.* **123**, 3256–3272 (2018). doi:10.1029/2018JE005820

230   13. M. Jia, et al., A catalogue of impact craters larger than 200 m and surface age analysis in the Chang'e-5 landing area. *Earth Planet. Sci. Lett.* **541**, 116272 (2020). doi:10.1016/j.epsl.2020.116272

14. Y. Qian et al. Young lunar mare basalts in the Chang'e 5 sample return region, northern Oceanus Procellarum, *Earth Planet. Sci. Lett.* **555**, 116-702 (2021).

235   15. D.T. Blewett, P.G. Lucey, B.R. Hawke, B.L. Jolliff, Clementine images of the lunar sample-return stations: Refinement of FeO and TiO2 mapping techniques. *J. Geophys. Res.* **102**, 16319–16326 (1997). doi:10.1029/97JE01505

16. Materials and methods are available as supplementary materials

17. C. R. Neal, L. A. Taylor, Petrogenesis of mare basalts: A record of lunar volcanism.

240   *Geochim. Cosmochim. Acta.* **56**, 2177–2211 (1992). doi:10.1016/0016-7037(92)90184-K

18. J. F. Snape, et al., The timing of basaltic magmatism at the Apollo lading sites. *Geochim. Cosmochim. Acta.* **266**, 29–53 (2019). doi:10.1016/ j.gca.2019.07.042

19. D.E. Moser, et al., Solving the Martian meteorite age conundrum using micro-baddeleyite and launch-generated zircon. *Nature* **499**, 454–457. doi:10.1038/nature12341

245   20. L.E. Borg, A.M. Gaffney, C.K. Shearer, A review of lunar chronology revealing a preponderance of 4.34–4.37 Ga ages. *Meteoritics*, **50** ,715-732 (2015). doi: 10.1111/maps.12373

21. D. S. Draper, et al., The Inner Solar System Chronology (ISOCHRON) Lunar Sample Return Mission Concept: Revealing Two Billion Years of History. *Planet. Sci. J.* **2**, 79

250   (2021). doi:10.3847/PSJ/abe419

22. W.K. Hartmann, C. Quantin, N. Mangold, Possible long-term decline in impact rates 2. Lunar impact-melt data regarding impact history. *Icarus* **186**, 11–23 (2007). doi:10.1016/j.icarus.2006.09.009

23. G. Neukum, B.A. Ivanov, W.K. Hartmann, Cratering records in the inner solar system in relation to the lunar reference system. *In: Chronology and Evolution of Mars. Space Sci. Rev.***96**, 55–86 (2001).

24. H. Hiesinger, C. H. van der Bogert, J. H. Pasckert, L. Funcke, L. Giacomini, L. R. Ostrach, M. S. Robinson, How old are young lunar craters? *J. Geophys. Res.* **117**, E00H10 (2012) doi:10.1029/2011JE003935

25. D. Stöffler, et al., Cratering History and Lunar Chronology in *New Views of the Moon,* B. L. Jolliff, M. A. Wieczorek, C. K. Shearer, C. R. Neal, Eds. (Mineralogical Society of America, Washington, D.C, 2006), *Rev. Mineral. Geochem.* **60***, pp. 519–596.

26. B. L. Jolliff, J. J. Gillis, L. A. Haskin, R. L. Korotev, M. A. Wieczorek, Major lunar crustal terranes: Surface expressions and crust-mantle origins. *J. Geophys. Res.* **105**, 4197–4216 (2000). doi:10.1029/1999JE001103

27. S. Marchi, S. Mottola, G. Cremonese, M. Massironi, E. Martellato, E., A new chronology for the Moon and Mercury. *Astron. J.* **137**, 4936–4948 (2009). doi:10.1088/0004-6256/137/6/4936.

28. http://www.cnsa.gov.cn/n6758823/n6758839/c6811124/content.html

29. J. D. Woodhead, J. M. Hergt, BCR/BHVO-Pb-Isotope Analyses of USGS Reference Materials. *Geostand. Geoanal. Res*. **24**, 33–38 (2000). doi:10.1111/j.1751-908X.2000.tb00584.x

30. N. Shimizu, S. R. Hart, Applications of the ion microprobe to geochemistry and
    cosmochemistry. *Annu. Rev. Earth Planet. Sci.* **10,** 483-526 (1982).
    doi:10.1146/annurev.ea.10.050182.002411

31. K. R. Ludwig, User's Manual for Isoplot 3.60, A geochronological toolkit for Microsoft
    Excel. *Berkeley Geochronol. Cent. Spec. Publ. 4*, Berkeley, California: Berkeley
    Geochronological Center. (2008)

32. K. P.Jochum, M. Willbold, I. Raczek, B. Stoll, K. Herwig, Chemical Characterisation of the
    USGS Reference Glasses GSA-1G, GSC-1G, GSD-1G, GSE-1G, BCR-2G, BHVO-2G and
    BIR-1G Using EPMA, ID-TIMS, ID-ICP-MS and LA-ICP-MS. *Geostand. Geoanal. Res.*
    29, 285-302 (2005). doi:10.1111/j.1751-908X.2005.tb00901.x

33. M. Elburg, P. Vroon, Sr and Pb isotopic composition of five USGS glasses (BHVO-2G,
    BIR-1G, BCR-2G, TB-1G, NKT-1G). *Chem. Geol.* 12 (2005). Doi:
    10.1016/j.chemgeo.2005.07.001

34. C. Gopel, G. Manhes, C. J. Allegre, U-Pb systematics in iron meteorites-Uniformity of
    primordial lead. *Geochim. Cosmochim. Acta.* **49**, 1681–1695 (1985). doi:10.1016/0016-
    7037(85)90139-5

35. J. Fritz, A. Greshake, D. Stöffler, Micro-Raman spectroscopy of plagioclase and
    maskelynite in Martian meteorites: Evidence of progressive shock metamorphism. *Antarct.*
    Meteorite Res. 18, 96-11(2005).

36. D. Stöffler, C. Hamann, K. Metzler, Shock metamorphism of planetary silicate rocks and
    sediments: Proposal for an updated classification system. *Meteorit Planet Sci.* Merrill R. B.
    and Papike J. J. New York: Pergamon Press. pp. 445–471. **53**, 5–49 (2018).
    doi:10.1111/maps.12912

37. J. J. Papike, F. N. Hodges, A. E. Bence, M. Cameron, J. M. Rhodes, Mare basalts: Crystal chemistry, mineralogy and petrology. *Rev. Geophys. Space Phys.* **14**, 475-540 (1976). doi:10.1029/RG014i004p00475

38. J. J. Papike, G. Ryder, C. K. Schearer, Lunar Samples in *Planetary Materials,* J. J. Papike, Eds. (Mineralogical Society of America, Washington, D.C, 2006), *Rev. Mineral. Geochem.* **36***,* pp. 5-01-5-189 (1998).

39. T. L. Grove, D. T.Vaniman, Experimental petrology of very low TI/VLT/basalts. in *Mare Crisium: the view from Luna 24*, R. B. Merrill, J. J. Papike, Eds. (New York: Pergamon Press), pp. 445–471 (1978).

40. G. J. Taylor, L. M. V. Martel, P. D. Spudis, The Hadley-Apennine KREEP basalt igneous province: The Hadley-Apennine KREEP basalt igneous province. *Meteorit. Planet. Sci*. **47**, 861–879 (2012). doi:10.1111/j.1945-5100.2012.01364.x

41. http://search.moondb.org/ database

42. T. J. Fagan, D. Kashima, Y. Wakabayashi, A. Suginohara, Case study of magmatic differentiation trends on the Moon based on lunar meteorite Northwest Africa 773 and comparison with Apollo 15 quartz monzodiorite. *Geochim. Cosmochim. Acta.* **133**, 97–127 (2014). doi:10.1016/j.gca.2014.02.025

43. M. A. Wieczorek, et al., The Constitution and Structure of the Lunar Interior. *Rev. Mineral. Geochem*. **60**, 221–364 (2006). doi:10.2138/rmg.2006.60.3

44. L. J. Hallis, M. Anand, S. Strekopytov, Trace-element modelling of mare basalt parental melts: Implications for a heterogeneous lunar mantle. *Geochim. Cosmochim. Acta.* **134**, 289–316 (2014). doi:10.1016/j.gca.2014.01.012

Author contributions:

XCh, AN, DL, MDN, BJ, KHJ, RT, JFS, JH, CRN designed the project. All authors contributed to writing lunar sample request application to CNSA. XCh, AN, DL, TL, ChW, MDN, BJ, KHJ, RT, JFS, MJW, ZhY, ChY, JL, ShX, ZB, RF, DL, ZL were involved in collecting analytical data. XCh, AN, DL, BJ, KHJ, RT, JFS, CRN, SGW produced tables, figures and made necessary calculations. AN, MDN, KHJ, RT, JH, JFS, BJ, CRN contributed to the writing of the original draft, and all authors were involved in editing and reviewing to produce the final version of the manuscript.

Competing interests: We declare no competing interests.

Data and materials availability: The lunar sample, designation CE5C0000YJYX03501GP, was provided by the China National Space Administration (CNSA) under a materials transfer agreement *(27)*. Two basalt fragments investigated here are currently held at the Beijing SHRIMP laboratory on a one-year loan (with a possibility of extension for another year), after which they will be returned to CNSA. Chang'e-5 samples may be requested from CNSA through a request procedure *(27)*. More details are provided in the supplementary materials. Our EMP data are provided in Data S1-S3, the Pb isotope results in Data S4, and the Raman measurements in Data S5-S6. Calculated bulk compositions of two fragments are given in Table S1

Supplementary Materials

Materials and Methods

Supplementary Text

Figs. S1 to S13

Table S1
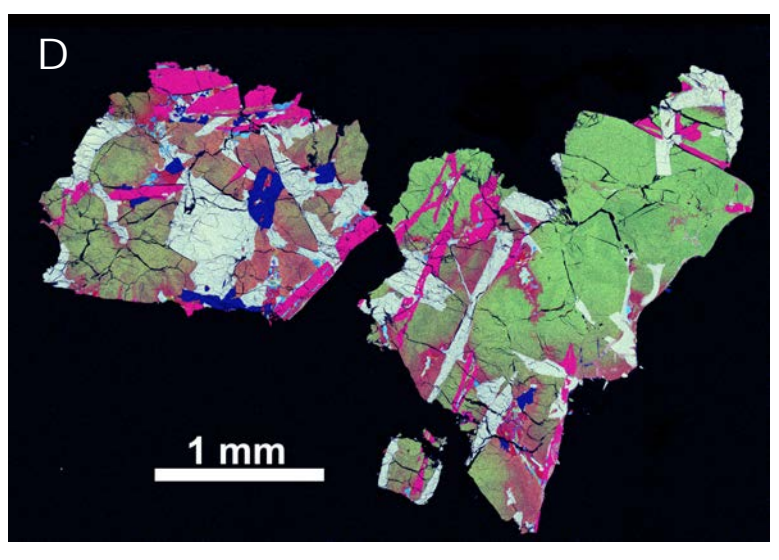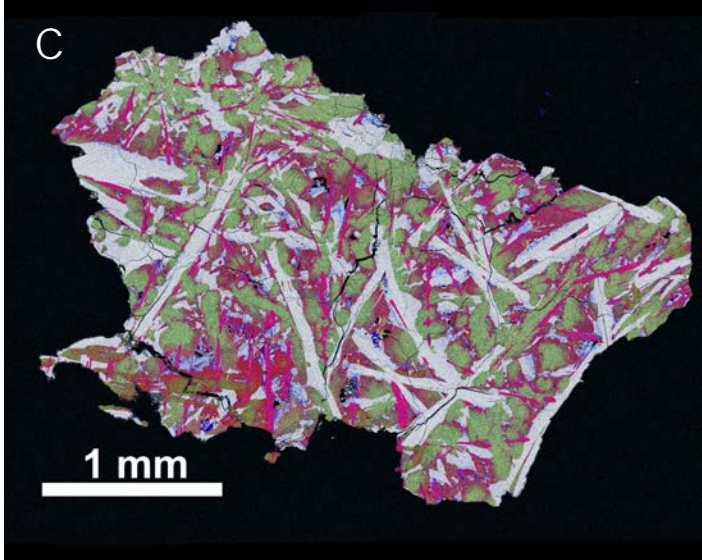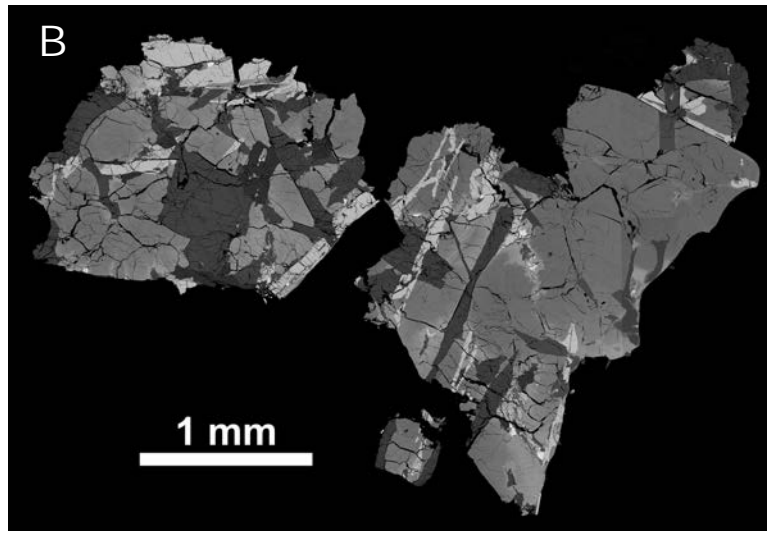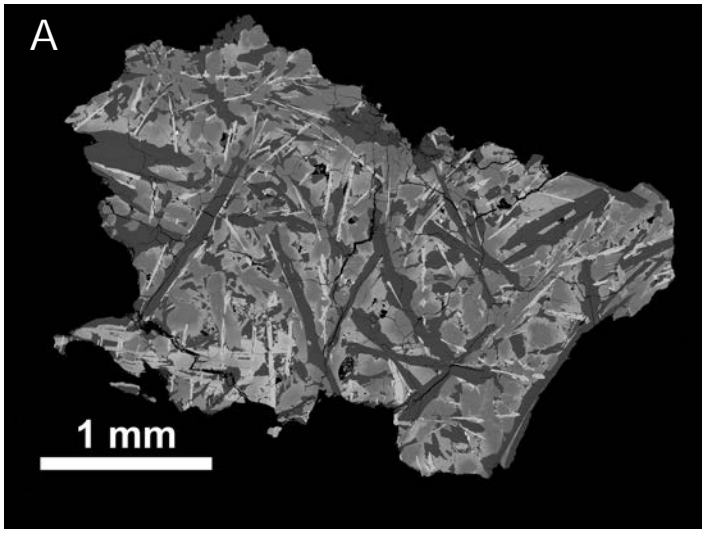
References (*29–44*)

Data S1 to S6

Figure 1. Back-scattered electron (BSE) images and false color energy dispersive spectroscopy (EDS) element maps of the two fragments from the Chang'e 5 sample. (A) and
365 (B): BSE images of CE-5-B1 and CE-5-B2, respectively. (C) and (D): EDS images of CE-5-B1 and CE-5-B2 (qualitative concentration and distribution of different elements in both samples are represented by different colours: blue=silica, green=Mg, red=Fe, white=Al, yellow=Ca, pink=Ti, cyan=K).
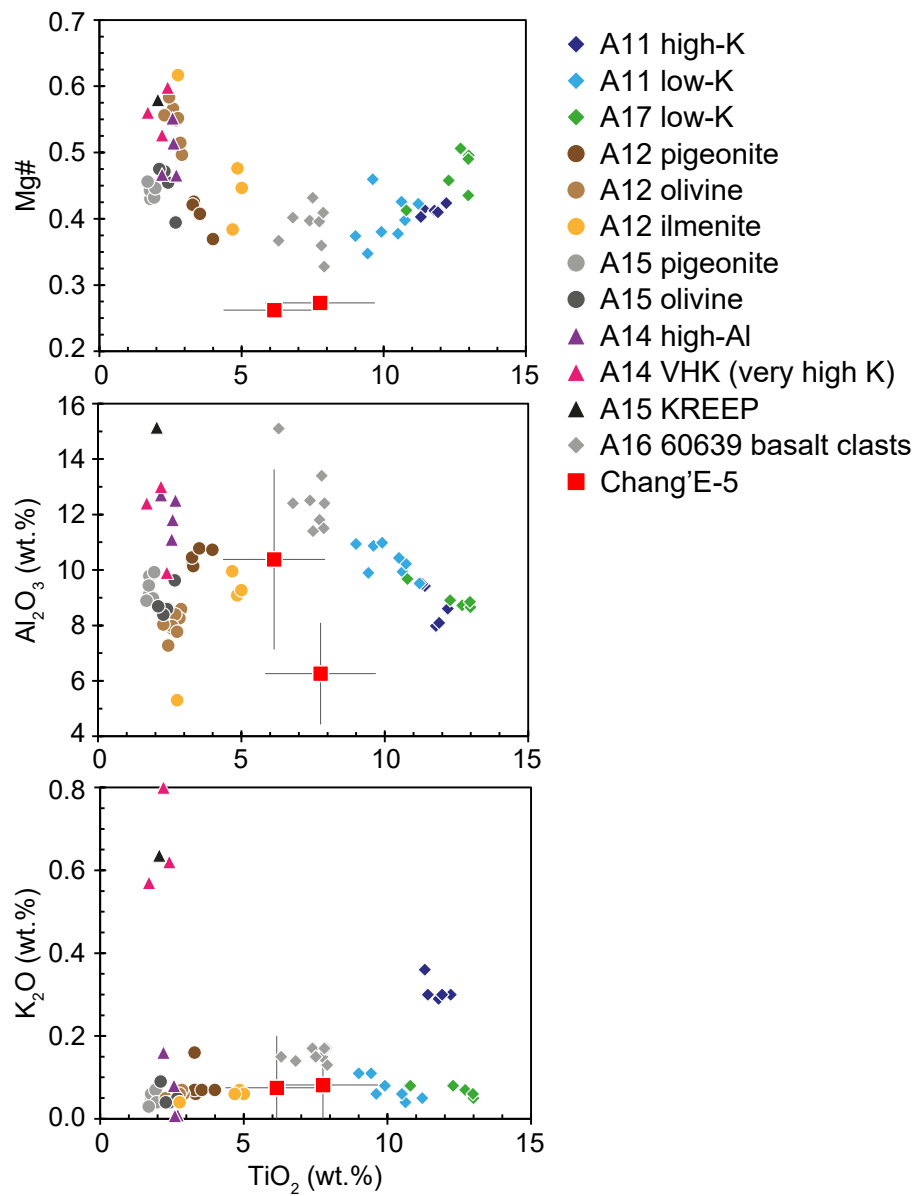
370 **Figure 2. Bulk chemical composition of basalt fragments.** Mg# (Mg/(Mg+Fe), Al_2O_3 and K_2O vs. TiO_2 plots for two analyzed Chang'e-5 fragments (red squares with 1 sigma error bars) compared to different basalts from Apollo landing sites (other symbols, as indicated in the legend, e.g. A11 stands for Apollo 11, A16 60639 refers to Apollo 16 sample 60639).

375 **Figure 3. Pb-Pb isotope data and isochrons for CE-5-B1 and CE-5-B2.** (A) Data for all measured points in the sample. Red points indicate analyses used to define the isochron, while grey points are analyses affected by terrestrial contamination. Black dot shows terrestrial Pb composition representing contamination. Blue dashed lines define mixing triangle (*16*), where steep line at the left is the isochron defining the age of the sample, line at the top is the best fit of
380 four K-feldspar analyses used to determine initial Pb composition, line at the bottom is mixing line with terrestrial Pb. MSWD is mean squared weighted deviation. (B) Analyses used to define the isochron: red data points are Zr minerals, light blue are phosphates, green are K-feldspar, black are K-glass. The blue lines show isochron constrained from all minerals (as in A) and the best fit line defined by analyses of Zr-rich minerals. All error crosses are at 2 sigma.

385

Figure 4. Lunar cratering chronology models compared to our measurement of the Chang'e-5 sample. Each model relates the radiometric and exposure ages of lunar samples to the frequency of 1-km impact craters $N(1)$ on each sampled unit. The Grey shaded areas indicate the age of Chang'e-5 basalt fragments determined in this study and range of $N(1)$ estimates for

390   the site from *(1, 3, 12, 13)*

Legend:
- A11 high-K
- A11 low-K
- A17 low-K
- A12 pigeonite
- A12 olivine
- A12 ilmenite
- A15 pigeonite
- A15 olivine
- A14 high-Al
- A14 VHK (very high K)
- A15 KREEP
- A16 60639 basalt clasts
- Chang'E-5

A

Lunar initial Pb

TerrestrialPb

Age = 1963 ± 57 Ma
MSWD = 1.3

$^{207}Pb/^{206}Pb$

$^{204}Pb/^{206}Pb$

B

Age = 1963 ± 57 Ma
MSWD = 1.3

Age = 2011 ± 50 Ma
MSWD = 1.5

$^{207}Pb/^{206}Pb$

$^{204}Pb/^{206}Pb$

range of N(1) in Chang'e 5 landing area

red- Neukum et al., 2001 *(23)*
blue solid- Marchi et al., 2009 *(27)*
blue dashd- Hartman et al, 2007 *(22)*
green- Robbins, 2014 *(5)*
pink- Draper et al., 2021 *(21 and references therein)*

Age of basalt fragments

$N(1)/km^{-2}$

Age (Ga)

Science

AAAS

Supplementary Materials for

Age and composition of the youngest basalts on the Moon as returned by the Chang'e-5 mission

Xiaochao Che, Alexander Nemchin*, Dunyi Liu*, Tao Long, Chen Wang, Marc D. Norman, Bradley Jolliff, Katherine H. Joy, Romain Tartese, Joshua F. Snape, James Head, Clive R. Neal, Martin J. Whitehouse, Carolyn Crow, Gretchen Benedix, Fred Jourdan, Zhiqing Yang, Chun Yang, Jianhui Liu, Shiwen Xie, Zemin Bao, Dapeng Li, Zengsheng Li, Stuart G. Webb

Correspondence to: liudunyi@bjshrimp.cn

a.nemchin@curtin.edu.au

This PDF file includes:

Materials and Methods
Supplementary Text
Figs. S1 to S13
Table S1

Other Supplementary Materials for this manuscript:

Data S1-S6

Materials and Methods

<u>Samples</u>

The Change'e-5 mission landed on 2020 December 1, at 43.06°N, 51.92°W in the Northern

35   Oceanus Procellarum region of the Moon, about 170km ENE of Mons Rümker, within

Procellarum-KREEP terrane (PKT). Remote sensing indicates that the main unit of relatively

young basalt flows (designated Em4/P58) (*1*) exposed around the landing site covers an area of

approximately 37000km^2 with a mean thickness of 51m and contains basalts with intermediate Ti

and high Th concentrations. The mission collected close to a total of 2 kg of core and scoop

40   samples and returned them to Earth on December 16.

Sub-sample CE5C0000YJYX03501GP containing two basalt fragments CE5-B1 and CE5-B2

mounted in a polished resin disc was prepared by the China National Space Agency (CNSA). We

applied to obtain this mount from CNSA in May 2021 and our request was granted in July. The

sample was subject to a material transfer agreement *(28)*.

45

<u>Initial sample imaging</u>

The sections were carbon coated and mapped using the Zeiss Merlin Compact Scanning Electron

Microscope (SEM) at the Beijing SHRIMP (Sensitive Hight Resolution Ion MicroProbe) Center,

Institute of Geology, Chinese Academy of Geological Sciences, Beijing, with a beam current of

50   6.6 nA and an accelerating voltage of 20 kV. The system was coupled to an Oxford X-Max^N 150

Energy Dispersive Spectroscopy (EDS) AZtec software to derive <1 μm per pixel back-scatter

electron (BSE) images and spatially-resolved element data (~0.38 μm per pixel). Each pixel of

data that is collected retains a complete 0-20 KeV energy spectrum and, therefore, we were able

to extract maps of O, Na, Mg, Al, Si, P, S, K, Ca, Ti, Cr, Mn, Fe and Ni, which provide an overview

55 of the compositional diversity and mineral phase location. Element maps were normalized to the

same brightness scale, colorised, and recombined to make qualitative false-color element maps

(Fig.1 C and D) using the ImageJ software package.

Electron probe microanalysis (EPMA)

60 Mineral and glass chemical compositions were analyzed using the Jeol JXA-8230 electron

microprobe at the Shandong Institute of Geological Sciences, Jinan. Analytical conditions used for

all analyses of different mineral phases and glass (voltage, beam current and spot size) are listed

in Data S1. Peak counting times were 10 to 40 s, and backgrounds were counted for half the

duration of peak counting time. Natural mineral standards were used to calibrate EPMA

65 measurements and included almandine, apatite, jadeite, kaersutite, pyrite, olivine, plagioclase,

pyrope, rutile, orthoclase and zircon. Accuracy of EPMA analyses was checked by repeated

analyses of selected Astimex standards, with SiO_2 within $\pm2.5\%$ of recommended abundances for

all silicates, Al_2O_3 within $\pm2.1\%$ for plagioclase, orthoclase, jadeite, pyrope, and almandine, TiO_2

within $\pm2.4\%$ for kaersutite, FeO within $\pm2.9\%$ for olivine, orthoclase, pyrope, almandine, and

70 kaersutite, MgO within $\pm1.8\%$ for olivine, pyrope, almandine, and kaersutite, MnO within $\pm15.9\%$

for pyrope, almandine, and kaersutite, CaO within $\pm2.8\%$ for plagioclase, pyrope, almandine, and

kaersutite, Na_2O within $\pm3.5\%$ for plagioclase and jadeite, K_2O within $\pm1.1\%$ for plagioclase,

orthoclase, and kaersutite, and Cr_2O_3 within $\pm4.9\%$ for pyrope (see Data S2).

All EPMA data are given in Data S1 and location of analytical spots are shown in Figures S1 and

75 S2, with average chemical compositions for each phase analyzed given in Data S3. The bulk

composition of each basalt fragment was estimated by modal recombination using BSE and EDS

X-ray images to obtain the fragments' modal compositions, and average EPMA compositions of

individual phases (Table S1). Modal compositions were determined by importing the images into the GNU Image Manipulation Program and using a combination of pixel brightness in the BSE

80   images and X-ray maps of characteristic elements to define the outlines of individual mineral phases. The pixel counts within these defined areas were then used to calculate final modal abundances. For bulk rock composition estimates, modal abundances of the different mineral and glass phases were converted in weight abundance using the following densities: 3.40 g/cm^3 for clinopyroxene, 4.07 g/cm^3 for olivine, 2.69 g/cm^3 for plagioclase, 2.62 g/cm^3 for silica, 4.72 g/cm^3

85   for ilmenite, 4.61 g/cm^3 for troilite, 2.56 g/cm^3 for K-feldspar, 2.70 g/cm^3 for K-rich glass, and 3.17 g/cm^3 for Ca-phosphates. The average composition of apatite was used for Ca-phosphates.

Raman analysis

Minerals were analyzed using the Horiba LabRAM HR Evolution Raman spectrometer at the

90   Beijing SHRIMP Center, Institute of Geology, Chinese Academy of Geological Sciences, Beijing, with a 532 nm laser excitation system (Nd: YAG).

An Olympus 100×/0.90 objective was used for all analysis, with ~1 μm laser spot sizes. The laser power was ~5 mW on baddeleyite and Ca-phosphate and ~20 mW on silicate minerals. The spectra were obtained in the range of 150-1500 cm^{-1}, with 1800 grooves/mm and 20 – 40 s

95   counting times. A silicon metal standard was used to calibrate the peak.

SHRIMP multicollector Pb-Pb isotopic analysis

The polished sections were cleaned in alcohol and distilled water, and gold-coated prior to Pb isotope analysis. Lead isotope data were collected using a SHRIMP IIe MC ion microprobe at the

100   Beijing SHRIMP Center, Institute of Geology, Chinese Academy of Geological Sciences, Beijing.

The mass filtered $^{16}O_2^-$ primary ion beam was reduced through a Köhler aperture of 70 μm to analyze some of the larger phosphate grains or 30 μm, which produced spot sizes of about 12 μm and 7 μm (primary beam 2.0 and 0.6 nA), respectively. Before each analysis, an area exceeding the analytical spot size by a few μm was pre-sputtered for 180 seconds. This pre-sputtering

105   removed the gold coating from the area around the analytical spot and limited the effects of surficial contamination. This procedure was followed by automatic centering of the secondary ion beam in the 80 μm source slit and automatic centering of the magnetic field. The secondary ions were measured using a static mode with four low-noise channel detection electron multipliers (CDEM). Baseline measurements were performed after analyzing Pb compositions in each spot.

110   Analyses of the BCR-2G USGS (United States Geological Survey) basaltic glass reference material (11 ppm of Pb) were used to generate correction factors to account for mass fractionation and detector relative gain calibration in the unknown analyses, assuming the values of *(29)* for Pb isotope ratios. This correction procedure involved dividing each of the "accepted" isotope ratios for BCR-2G (determined independently using TIMS (thermal ionization mass spectrometry)

115   analyses *(29)* by the corresponding average of each ratio obtained from all standards in the session in order to obtain a ratio-specific correction factor that incorporates both mass bias (a few parts per thousand at Pb mass; *30)* and detector gains (a few percent). Measured isotope ratios of the unknowns were then corrected by multiplying by these factors. There was a major instability of the instrument during the session, which required a retuning and resulted in a change of collectors'

120   gains. Consequently, two separate sets of BCR-2G analyses were used to correct unknowns before and after retuning. Within uncertainty limits, no systematic drift was observed in the BCR-2G measurements within these two sets, with the 1σ standard deviations for isotope ratios all being

less than 1%. The complete set of BCR-2G analyses is reported in Data S4 and shown in Figure S3.

125   The uncertainties stated for each ratio in the individual sample measurements were derived from the internal run uncertainty propagated together with the standard deviations of the BCR-2G analyses for the relevant set and the uncertainty given for the published BCR-2G values (*29*). The uncertainties stated for the Pb-Pb isochron dates are quoted at the 95% confidence level while errors of individual analyses in Data S4 are presented at 1 sigma level and plotted at the 2 sigma

130   level in all figures.

Reduction of the SHRIMP data was done manually in Excel. Final age calculations and plots were made using the Isoplot Excel add-in (version 4.15; *31*).

To assess the accuracy of the Pb isotope analyses and provide additional means to monitor stability of the instrument during the session, a second USGS reference sample (BHVO-2G) was run

135   frequently after several analyses of lunar sample. This reference sample has an order of magnitude lower Pb concentration compared to BCR *(32)* and approximates some low Pb abundance phases often present in lunar basalts. The data obtained for BHVO-2G corrected for backgrounds and gains are presented in Data S4 and shown in Figure S4. The data set combines all analyses made before and after instrument retuning and the absence of visible change in Pb compositions

140   throughout the full session (Fig. S4) demonstrates that gain correction using the BCR primary standard is adequate to obtain true values for isotopic ratios. These true values are within the uncertainties of independently determined ratios *(33)*.

Pb-Pb data processing

145 All SHRIMP analytical spots are shown in Figures S5 and S6. The data were processed using in-house data reduction spreadsheets and the Excel add-in Isoplot (version 4.15; *31)*, using previously established methods *(18)*. The Pb isotopic compositions measured in individual spots are interpreted as representing a mixture between three main components: (i) initial Pb present in the basaltic melt when it crystallized, (ii) radiogenic Pb formed by the decay of U after crystallization,

150 and (iii) terrestrial contamination. These end-member components define a triangular array of points on a plot of $^{207}Pb/^{206}Pb$ vs. $^{204}Pb/^{206}Pb$ (e.g., Fig. 3A). The values with the highest $^{207}Pb/^{206}Pb$ ratios, at the top of the triangular array, provide an estimate of the lowest possible value for the initial Pb composition of the sample. The radiogenic Pb component is located where $^{204}Pb/^{206}Pb = 0$. Finally, given the very radiogenic Pb isotopic compositions associated with the

155 Moon relative to those found on Earth, the terrestrial contamination endmember will have the highest $^{204}Pb/^{206}Pb$ ratios. Based on this assumption, the bounding edge on the left side of the triangle, between the initial and radiogenic lunar Pb compositions, forms an isochron, which can be determined by iteratively filtering the data to yield the steepest statistically significant weighted regression (i.e., Mean Squared Weighted Deviation, MSWD < 2; probability of fit, P > 0.05).

160 Pb concentrations (Data S4) were estimated using Pb counts obtained for each spot divided by mean counts determined in BCR and multiplying by Pb concentration in BCR. U and Th isotopes were not measured directly; estimates for U and Th concentrations as well as Th/U ratios have been made assuming concordance of U-Th-Pb systems using the Pb-Pb isochron age of the fragments.

165 The basalts source $^{238}U/^{204}Pb$ (μ-value) can be assessed using either one or two stage model. The first model assumes that Pb isotopes evolve in a basalt source from the time of Moon (t_0) formation and primordial Pb composition determined to be close to Pb measured in Canyon Diabolo Troilite

(CDT) *(34)* to the time of basalt formation (t_b). In this case initial Pb compositions measured in basalt samples can be expressed as: [check symbols below – some subscripts may not reproduce in Word files]

$$\frac{^{206}Pb}{^{204}Pb}\bigg|_{initial\ in\ basalt} = \frac{^{206}Pb}{^{204}Pb}\bigg|_{CDT} + \mu * (exp^{\lambda_{238}*t_0} - exp^{\lambda_{238}*t_b})$$

$$\frac{^{207}Pb}{^{204}Pb}\bigg|_{initial\ in\ basalt} = \frac{^{207}Pb}{^{204}Pb}\bigg|_{CDT} + \frac{\mu}{137.88} * (exp^{\lambda_{235}*t_0} - exp^{\lambda_{235}*t_b})$$

Where λ_{238} and λ_{235} are decay constants of ^{238}U and ^{235}U and 137.88 is natural ^{238}U/^{235}U

The μ-value can be estimated from either or both of these equations.

In contrast, the two-stage model assumes that an early (first) stage is associated with initial crystallization of Lunar Magma Ocean after formation of the Moon, and a second stage associated with a later internal reorganization of the Moon possibly associated with convective overturn. This first stage takes place from t_0 (and CDT composition) to the end of LMO crystallization t_{LMO}, which is also the time of basalt source formation. The second stage evolves Pb from t_{LMO} to t_b. For the two-stage model the equations change to:

$$\frac{^{206}Pb}{^{204}Pb}\bigg|_{initial\ in\ basalt} = \frac{^{206}Pb}{^{204}Pb}\bigg|_{CDT} + \mu_{LMO} * \left(exp^{\lambda_{238}*t_0} - exp^{\lambda_{238}*t_{LMO}}\right) + \mu * (exp^{\lambda_{238}*t_0} - exp^{\lambda_{238}*t_b})$$

$$\frac{^{207}Pb}{^{204}Pb}\bigg|_{initial\ in\ basalt} = \frac{^{207}Pb}{^{204}Pb}\bigg|_{CDT} + \frac{\mu_{LMO}}{137.88} * (exp^{\lambda_{235}*t_0} - exp^{\lambda_{235}*t_{LMO}}) + \frac{\mu}{137.88} * (exp^{\lambda_{235}*t_0} - exp^{\lambda_{235}*t_b})$$

Where μ_{LMO} is μ of Lunar Magma Ocean. Both μ and μ_{LMO} can be estimated from two equations.

Supplementary Text

<u>Detailed Petrography and Mineral Chemistry</u>

CE-5-B1

CE-5-B1 is a fine-grained subophitic mare basalt (Fig. 1). The section we received CNSA has some small adhering regolith particles. The fragment is cross-cut by fractures (~1-10 microns in width) but has no obvious shock melt pockets or veins (Fig. S7a). The area modal mineralogy is estimated to be 51.2% augite, 34.4% plagioclase, 4.8% olivine, 6.7% ilmenite, 1.0% silica, 0.3% troilite, 0.6% K-rich glass, 0.5% Ca-phosphates (apatite and merrillite), and trace amounts of K-feldspar (Table S1).

Pyroxene occurs as small (up to 600 µm in length) grains that partially enclose other minerals in the sample. They are zoned from Mg-Ca rich cores to highly fractionated Fe-rich and Ca-poor pyroxferroite rims (En_{1-43}, Fs_{27-86}, Wo_{13-41}) (Fig. S8), and have FeO/MnO ratios (52 to 86) typical of lunar basalts. Plagioclase occurs as elongate laths, up to ~1 mm in length and 300 µm in width. Several grains have hollow cores, similar to some Apollo 'intrafasciculate' or variolitic mare basalts. The grains are cross-cut by micron-scale microfractures (Fig. S7a), but are internally smooth with no crackled appearance, suggesting that the grains could have been partially to totally transformed to maskelynite. Nevertheless, this observation is not supported by Raman investigation of several plagioclase grains in the sample (Fig. S9), where half of 14 Raman spectra obtained in the sample (Fig. S10) show a pronounced peak at around 570 cm^{-1}, suggesting unmodified crystalline plagioclase. This peak is less pronounced in the rest of the obtained spectra, showing lower intensity, but no apparent broadening or shift of this band, which could be taken as an indication of a very mild shock. Even if these observations are interpreted as resulting from the shock the P would not exceed 20 to 25 GPa *(35)*. Plagioclase is chemically zoned with a range of

compositions from An_{81-91}, Ab_{8-18}, $Or_{0.6-2}$ (Fig. S11). Some plagioclase rims adjacent to the late-stage mesostasis assemblages have micro-inclusions of K-feldspar. Olivine grains are irregular in size and shape, often skeletal, and are sometimes intersected by ilmenite crystals. Olivine grains are gradually zoned from Fo_{44} to Fo_6 (Fig. S8), where the most fayalitic portions are adjacent to the mesostasis pockets. Olivine FeO/MnO ratios (82 to 100) are typical of lunar basalts. Ilmenite are needle-like, up to ~800 μm in length, often have a skeletal appearance with some hollow cores, and are relatively homogenous, with low MgO concentrations (<0.34 wt%). Mesostasis assemblages include K-feldspar, which is Ba-bearing (10.3-13.8 wt% BaO). Also present are silica grains (undetermined polymorph, up to ~60 μm in size), Ca-phosphates merrillite and apatite, troilite, and immiscible textures of Si-Al-K rich glass (which is Ba-bearing with up to 1 wt% BaO, but is P_2O_5 poor), fayalite, and silica (Fig. S4b).

CE-5-B2

CE-5-B2 is a coarser-grained (relative to CE-5-B1) subophitic mare basalt. The fragment is more fractured than CE-5-B1, with most mineral phases displaying highly fractured textures. Shock melt pockets and veins (a few tens of microns wide) are present in one portion of the sample (Fig. S4c, also see composition reported in Data S1), suggesting high-P and high-T deformation indicative of localized shock pressures of >60 GPa *(36)*. However, Raman investigation of minerals in the fragment (Fig.S10) indicates that this shock was localized in one corner of the fragment (Fig. S9). Maskelynite is only present in this corner of the fragment where shock-produced glass can be seen (Fig. S9). All other Raman spectra are similar to those observed in CE-5-B1and indicate predominantly unshocked crystalline plagioclase. One possible exception is spot B2-19 (Fig.10), which shows broadening and shift of 570cm^{-1} band indicating possible shock up to about 30 GPa *(35)*. However, this spot is located at the boundary between the unmodified part of the fragment

and the area where shock melt is identified (Fig.S9). All other minerals in the fragment show no indication of any modification by shock in their Raman spectra (Fig.S10).

The area modal mineralogy is estimated to be 64.6% augite, 20.0% plagioclase, 1.9% olivine, 9.3% ilmenite, 2.2% silica, 0.4% troilite, 0.7% K-rich glass, 0.4% Ca-phosphates (apatite and merrillite) and 0.1% K-feldspar (Table S1).

Pyroxene occurs as grains up to ~ 2 mm in size that partially enclose other minerals in the sample. These grains are zoned from Mg-rich cores to higher Fe-rich pyroxferroite rims (En_{4-42}, Fs_{26-73}, Wo_{19-42}) (Fig. S8), where the rim areas are smaller and more sharply defined from the cores than those in CE-5-B1. The pyroxene grains have FeO/MnO ratios (51 to 74) typical of lunar basalts. Plagioclase occurs both as blocky crystals (up to ~750 μm in length) with some longer lath-like grains (up to ~1.2 mm in length). The grains are cross-cut by micron-scale microfractures, and internally have a crackled appearance, suggesting brittle deformation. Plagioclase is chemically zoned with An-rich cores, and a total compositional range of An_{74-94}, Ab_{5-21}, $Or_{0.2-5}$ (Fig. S11). Olivine is less common in CE-5-B2 than in CE-5-B1, occurring only in one portion of the section. Here the olivines are gradually zoned from Fo_{43} to $Fo_{0.7}$ (Fig. S8), where the most fayalitic portions are adjacent to the mesostasis pockets. Olivine FeO/MnO ratios (82 to 100) are typical of lunar basalts. Ilmenites are a mix of blocky and needle-like grains, up to ~800 μm in length, and are relatively homogenous with low MgO concentrations (<0.93 wt%). Silica grains (undefined polymorph) are blocky, up to 400 μm in length, and significantly coarser grained than in CE-5-B1. Late-stage melt pockets are less common than in CE-5-B1, but there are some small areas of mesostasis (Fig. S7d) with Si-Al-K-rich glass (which is Ba-bearing with up to 1.9 wt% BaO, but is P_2O_5 poor), fayalite, troilite, Ca-phosphates merrillite and apatite, and Zr-rich phases.

<u>Petrogenetic relationships between the fragments and comparison to Apollo mare basalts.</u>

Both the CE-5-B1 and CE-5-B2 basalts exhibit strong Fe-enrichment mineral chemistry patterns indicating extreme fractional crystallization (Fig. S8). Pyroxene compositions in the two basalt fragments are augitic and are more akin to those seen in high-Ti mare basalts, than those in low-Ti basalts, where the latter tend to be dominated by pigeonite. Trends of Al/Ti (cation ratio) vs Fe# (Fe/(Fe+Mg)) (Fig. S12b), indicate that pyroxene, plagioclase, and ilmenite were all co-crystallizing phases, suggesting that like in Apollo high-Ti basalts, ilmenite was an early crystallizing phase and continued to crystallize all through the crystallization sequence (see also *37-39*). Trends of Ti# (Ti/(Ti+Cr)) vs Fe# (Fe/(Fe+Mg)) indicate that both the CE-5-B1 and CE-5-B2 fragments did not co-crystallize with any Cr-bearing spinel, and again are more compositionally similar to high-Ti mare basalts than low-Ti basalts (Fig. S12a). The cores of the CE-5-B1 pyroxene are TiO_2- and Cr_2O_3-poorer (1.1-2.3 TiO_2 wt%, 0.25-0.44 Cr_2O_3 wt%) than in CE-5-B2 pyroxene (2.55-3.9 TiO2 wt%, 0.39-0.47 Cr2O3 wt%) (Fig. S12c and d), indicating that CE-5-B2 may have crystallized from a slightly Ti and Cr-richer parent melt than CE-5-B1.

The cores of pyroxene crystals are more magnesian (Mg# (CE-5-B1) =56, Mg# (CE-5-B2) =59) than the cores of olivine crystals (CE-5-B1 olivine is Fo_{44} and CE-5-B2 olivine is Fo_{43}) (Fig. S12), where Mg# is Mg/(Mg+Fe) and Fo (forsterite) refers to the proportion of pure Mg-olivine. This could suggest that pyroxene was the earlier crystallizing phase, or that more forsteritic olivine is not preserved in the sample we have analyzed. The olivine cores are also more ferroan than the earliest crystallizing olivine in Apollo mare basalts and lunar meteorite crystalline basalts, and in the basalt fragments found in the Apollo 16 sample 60639 *(40)* (Fig. S12). Using the relationship between melt composition and expected precipitating mineral phases, i.e.
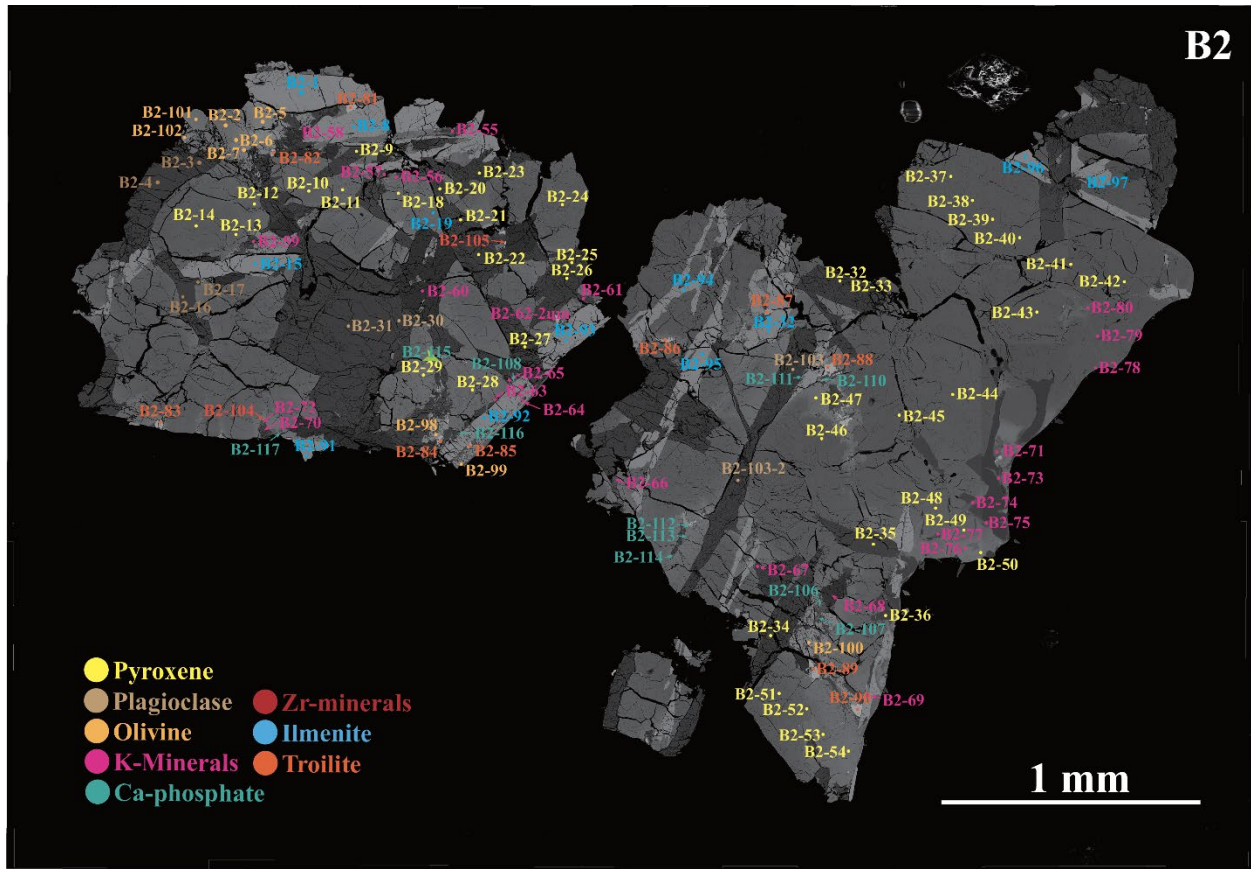
$$Mg\#(melt) = \cfrac{1}{\cfrac{\left(\frac{1}{Olivine\ Fo}-1\right)}{Kd}+1}$$

and assuming a mare basalt relevant Kd (partition coefficient) of 0.33 *(39)*: the most Mg-rich olivine in CE-5-B1 (Fo_{44}) precipitated from an equilibrium parent melt with a Mg# composition of 21, and most Mg-rich olivine in CE-5-B2 (Fo_{43}) precipitated from an equilibrium parent melt with a Mg# composition of 20. These modelled compositions are similar to the bulk rock composition (Mg# (CE-5-B1) = 26.2 and Mg# (CE-5-B2) =27.3: Table S1).

The ferroan nature of ferro-magnesian minerals in the Chang'e-5 fragments is reflected in whole rock bulk estimates that suggest that the studied Chang'e-5 basalts have higher FeO and lower MgO abundances than most lunar basalts studied to date (Fig. S13). They also have low Cr_2O_3 compared to most mare basalts.
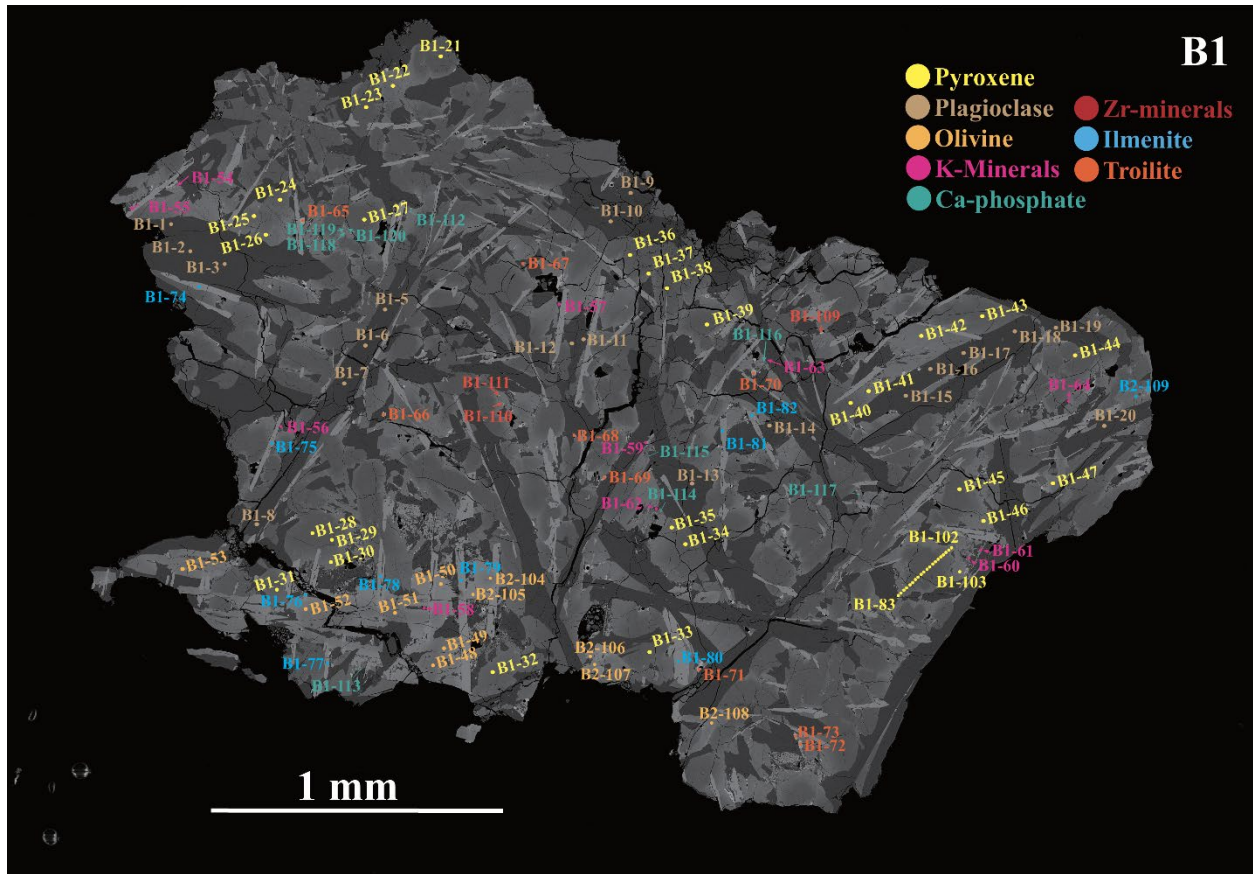
Fig. S1. Location of EMPA spots in the basalt fragment CE5-B1. EMPA spots in different minerals are shown in different color. Strings of spots looking like dotted lines represent profiles across individual grains of some minerals. Labels next to spots correspond to the numbers in the table (Data S1)

295

**Fig. S2. Same as figure S1, but for basalt fragment CE5-B2**

A

204 Pb/206 Pb

Mean = 0.05438±0.00048 (95% conf.MSWD= 2.0),

D

204 Pb/206 Pb

Mean = 0.06135±0.00060 (95% conf.MSWD= 0.7

B

207 Pb/206 Pb

Mean = 0.8365±0.0026 (95% conf MSWD= 2.1)

E

207 Pb/206 Pb

Mean = 0.8091±0.0049 (95% conf MSWD= 2.6)

C

208 Pb/206 Pb

Mean = 2.0743±0.0061 (95% conf.MSWD= 3.0)

F

208 Pb/206 Pb

Mean = 2.002±0.011(95% conf.MSWD= 2.9)
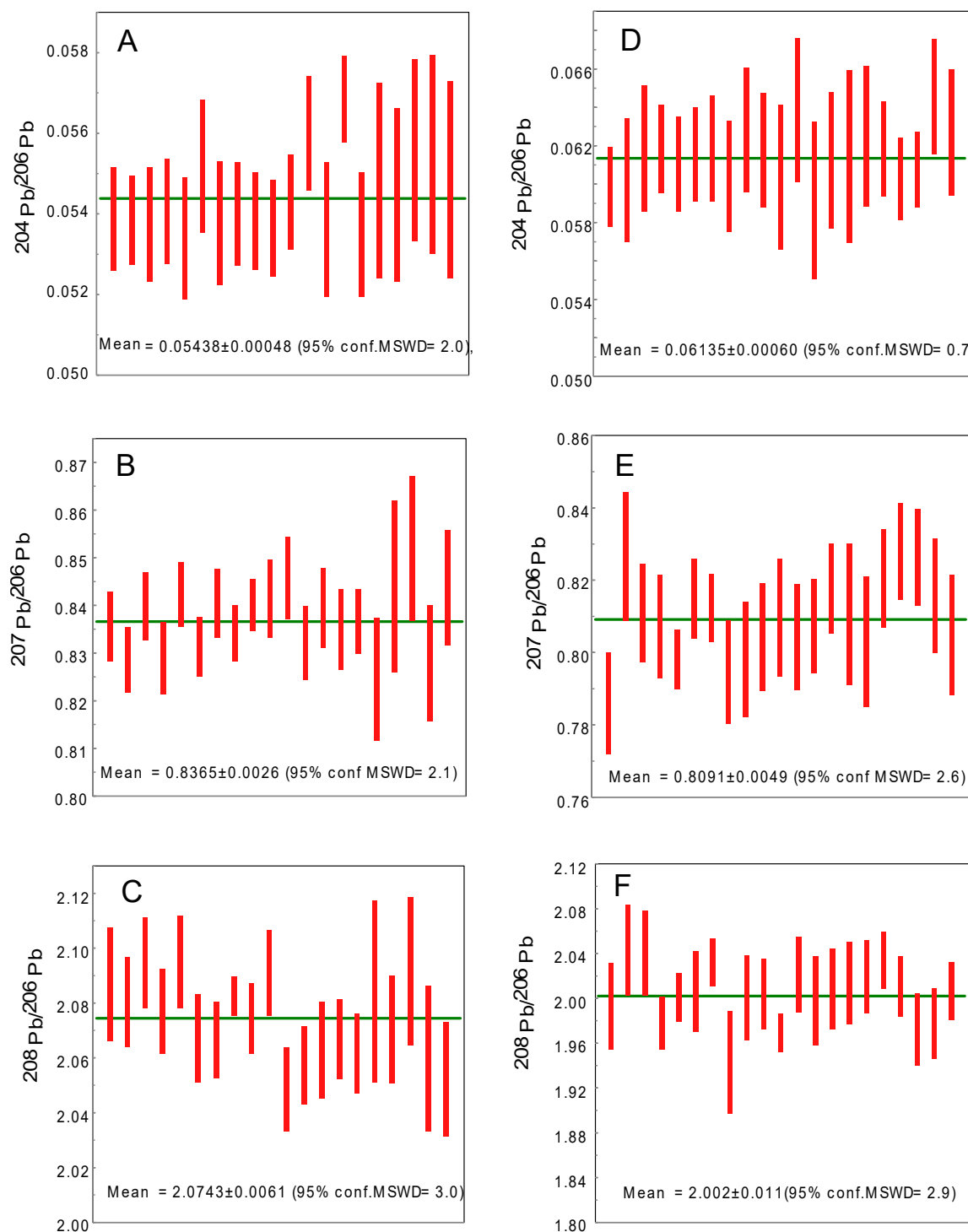
Fig. S3. Lead isotope analyses of BCR-2G obtained during the analytical session.
A, B and C are three Pb isotope ratios measured before instrument retuning. D, E and F are same
ratios measured after retuning. Analyses are arranged sequentially along the horizontal axis.
Length of red bars is 2 sigma error. Green line represents weighted mean of all analyses. MSWD
is mean squared weighted deviation
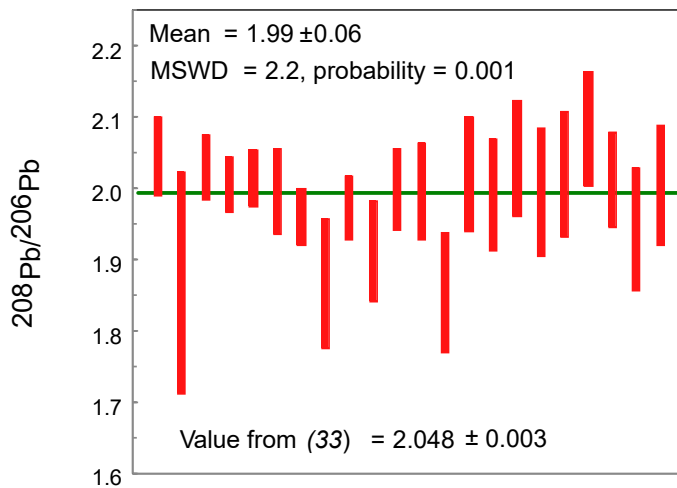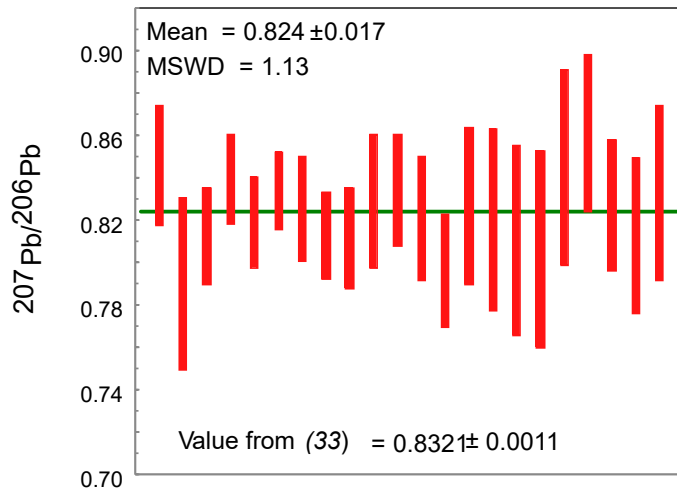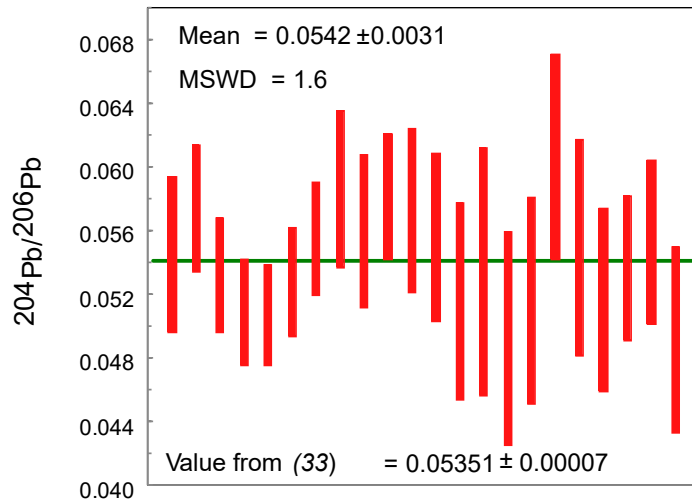
Fig. S4. Same as figure S3, but for the BHVO-2G reference glass. Collectors' gains were corrected using repeated analyses of BCR-2G (see text for details). Independently determined values for Pb isotope ratios by *(33)* are shown on each diagram.
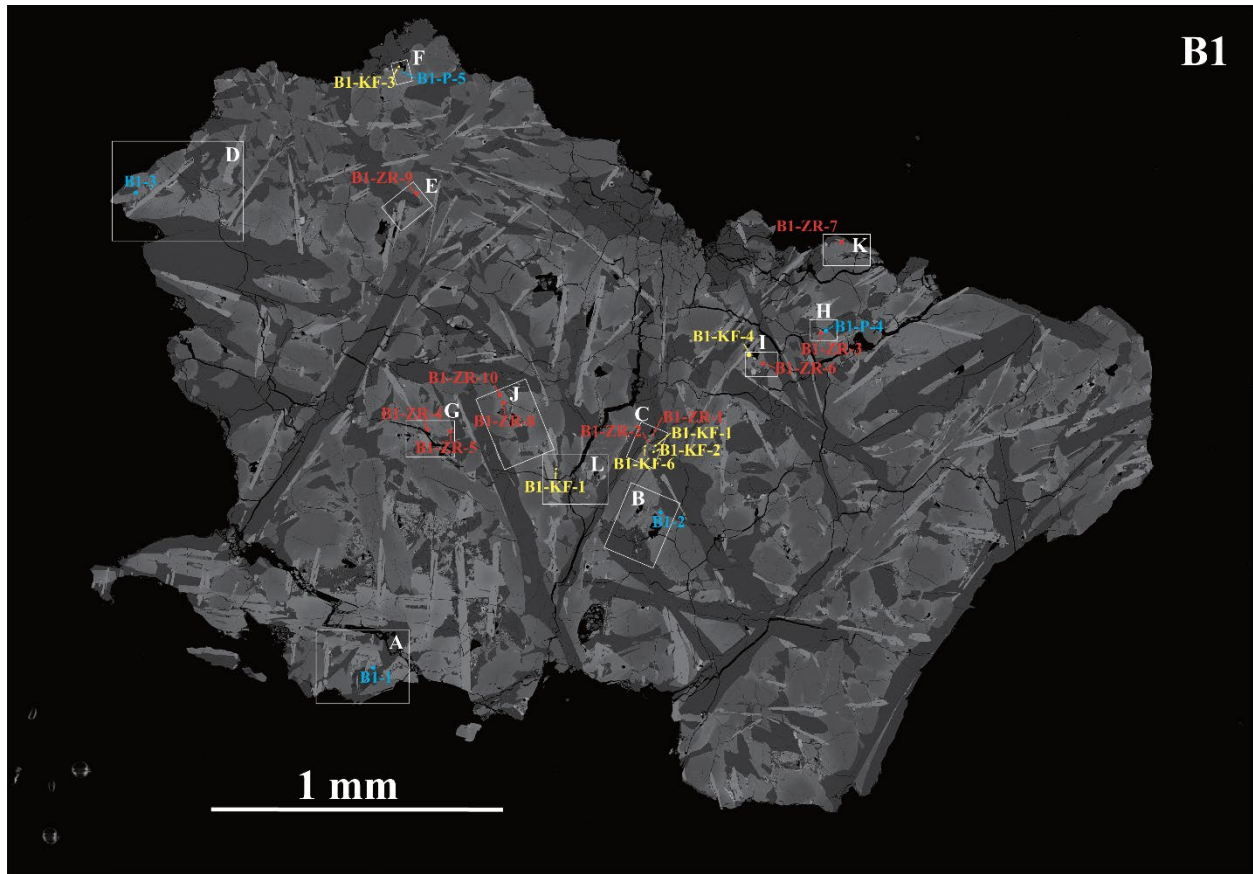
310

Fig. S5. Location of SHRIMP spots in the fragment CE5-B1

Colors indicate different phases (Zr- minerals- red; phosphates – blue and K-phases – yellow). Labels correspond to numbers in the data table (Data S4). White rectangles with labels show locations of zoomed individual areas showing textural context for each analyzed spot

315
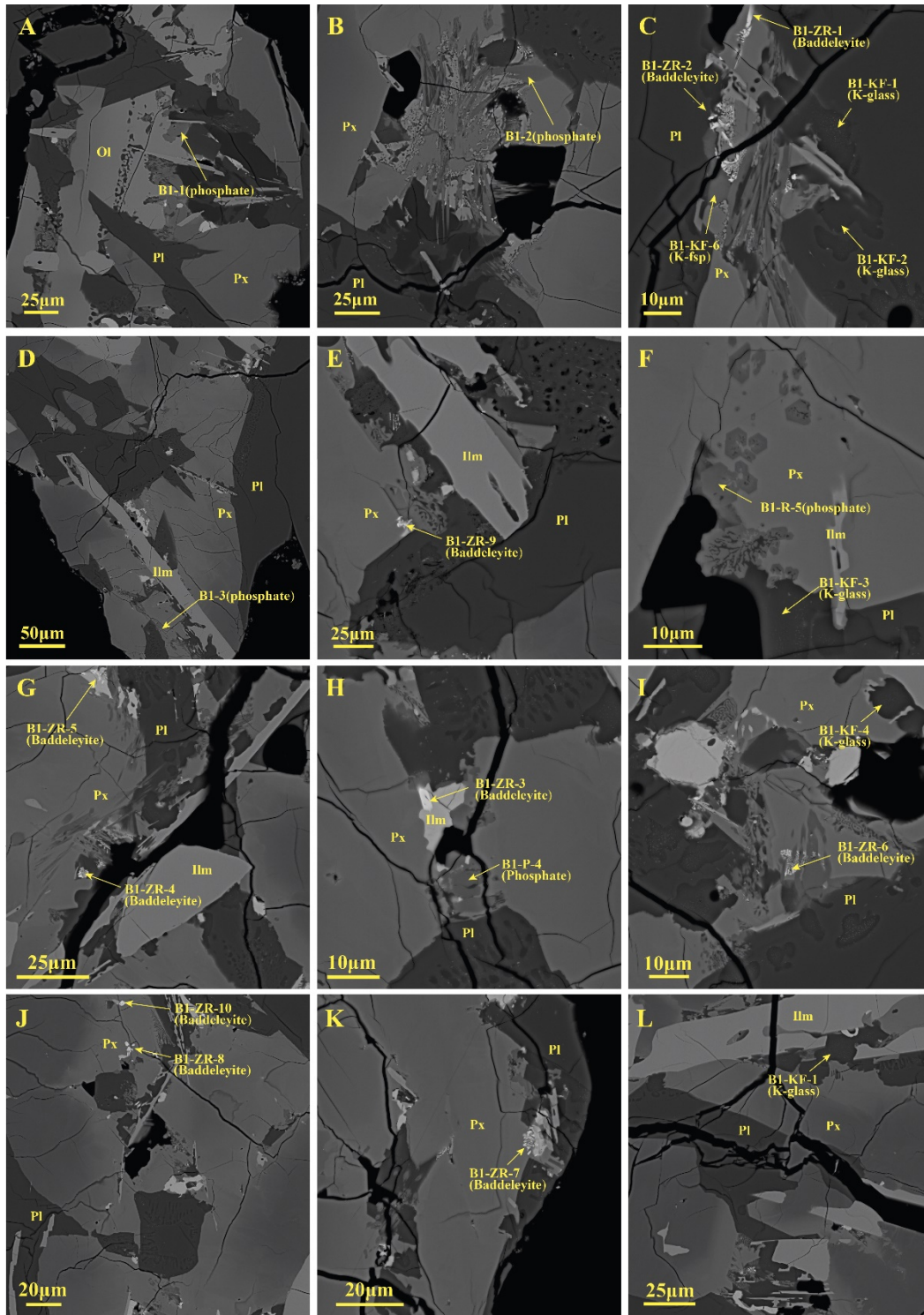
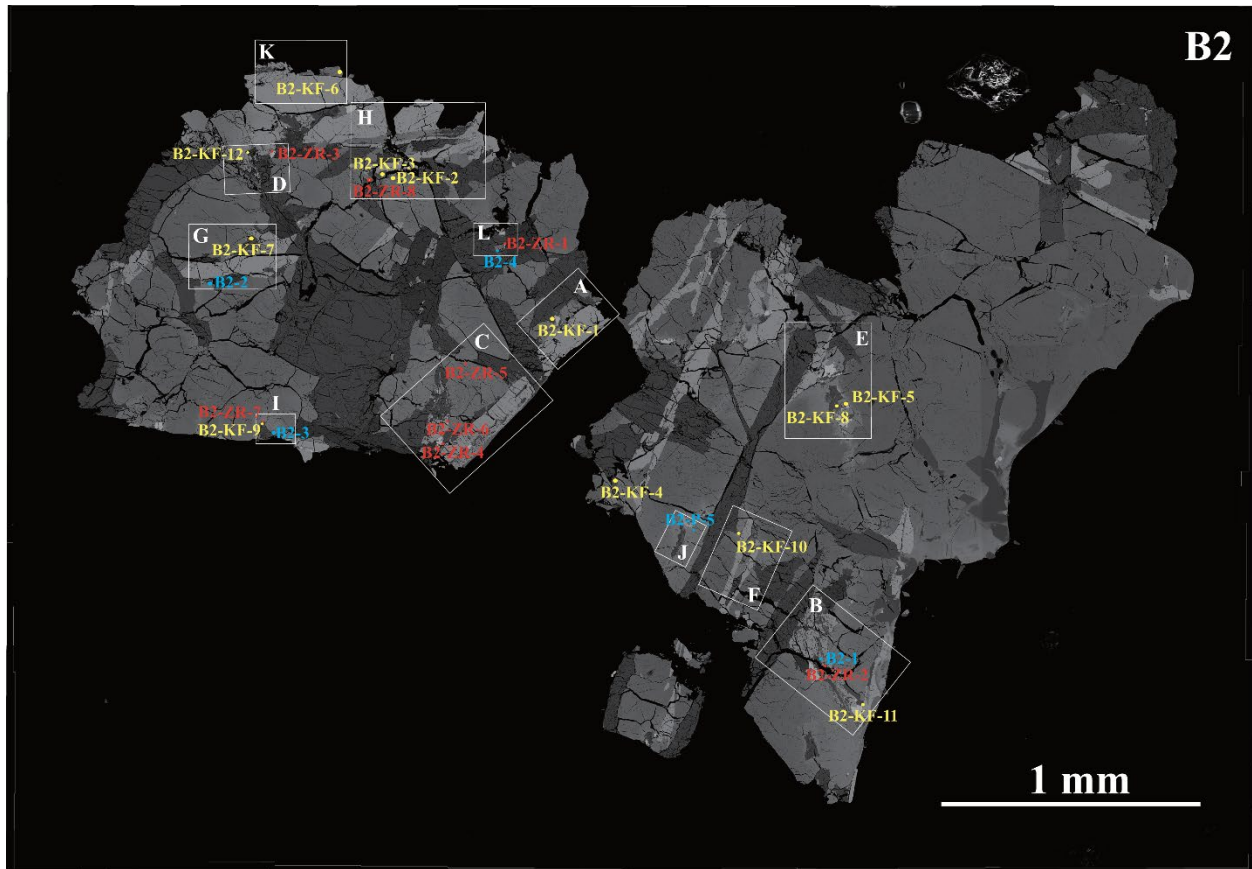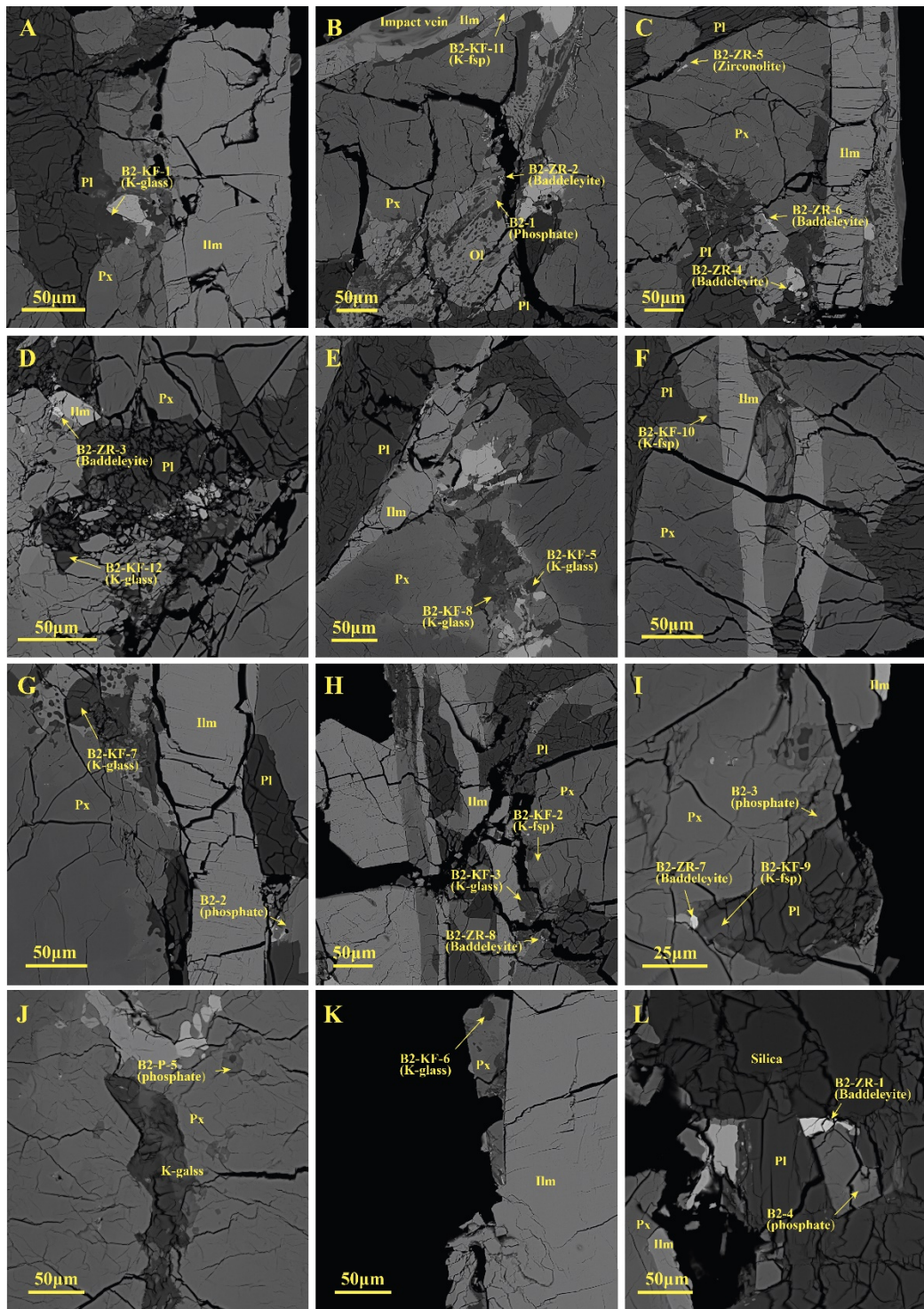**Fig. S5 (continued)** Zoomed areas showing analytical spots. Labels indicate different minerals (Pl-plagioclase; Px-pyroxene; Ilm – ilmenite)
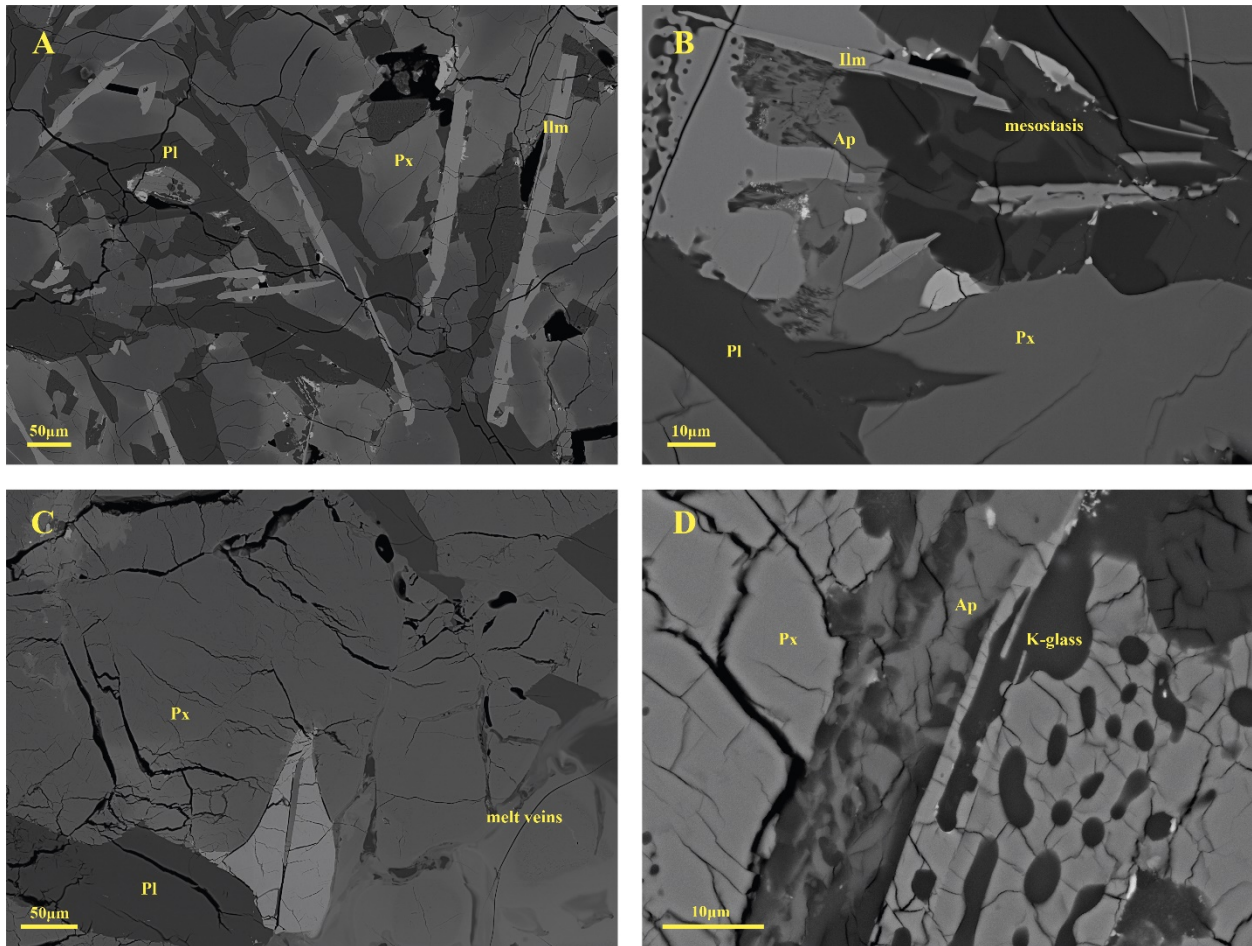
Fig. S6. Same as figure S5, but for the fragment CE5-B2

Fig. S6 (continued)

Fig. S7. Enlarged areas in analyzed samples showing common textural features of two fragments.

BSE images of selected areas showing: (A) fracturing in CE5-B1; (B) mesostasis in CE5-B1; (C) impact melt zone in CE5-B2; (D) mesostasis in CE5-B2. Labels indicate different minerals (Pl-plagioclase; Px – pyroxene; Ilm – ilmenite; Ap – apatite; K-glass – potassium rich glass)
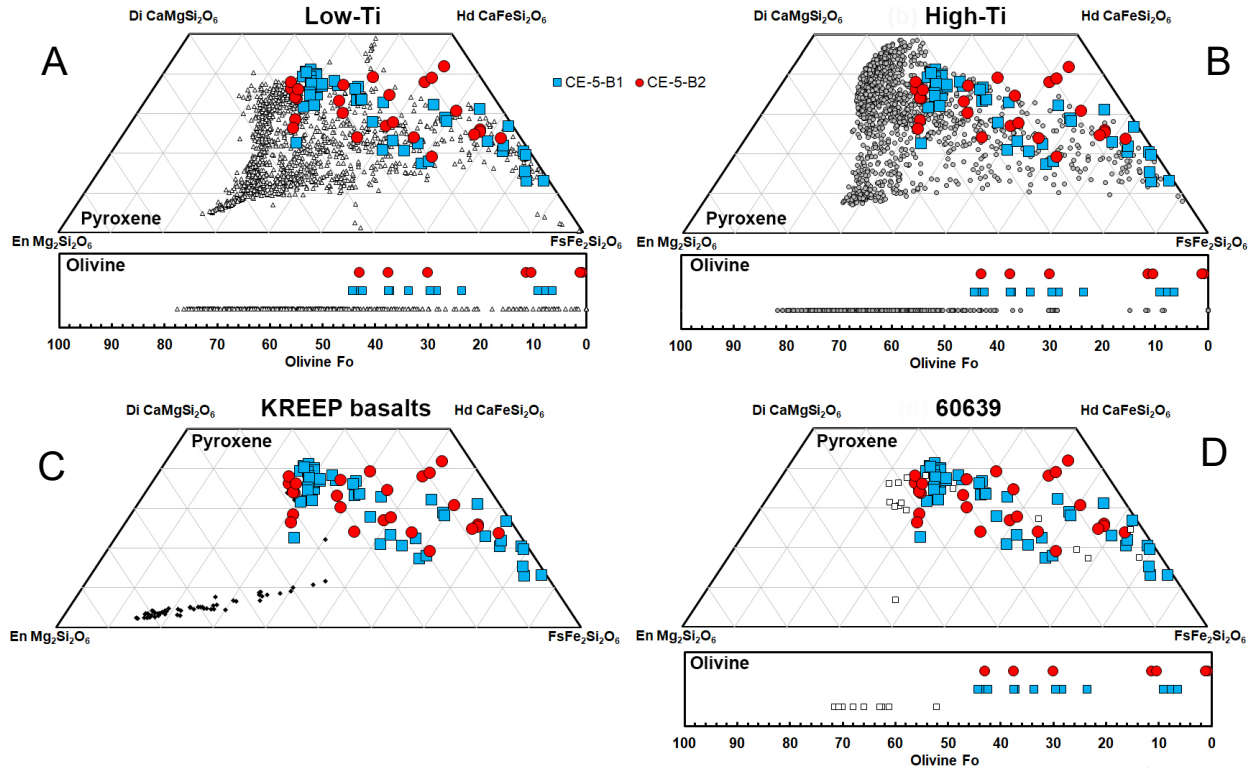
Fig. S8. Chemistry of pyroxene and olivine in two analyzed fragments.

340　Pyroxene and Olivine (Fo#-proportion of forsterite in olivine) mineral chemistry in basalt fragments CE-5-B1 (blue symbols) and CE-5-B2 (red symbols). Data are compared with (A) Apollo low-Ti mare basalts from the Apollo 12 and 15 landing sites *(41)*; (B) Apollo high-Ti mare basalts from the Apollo 11 and 17 landing sites *(41)*. (C) KREEP basalts *(41)* and from *(40)* (olivine values for KREEP basalts are not available to be compared). (D) Intermediate-Ti basalt

345　fragments in sample 60639 *(42)*. All Apollo data are shown as grey symbols
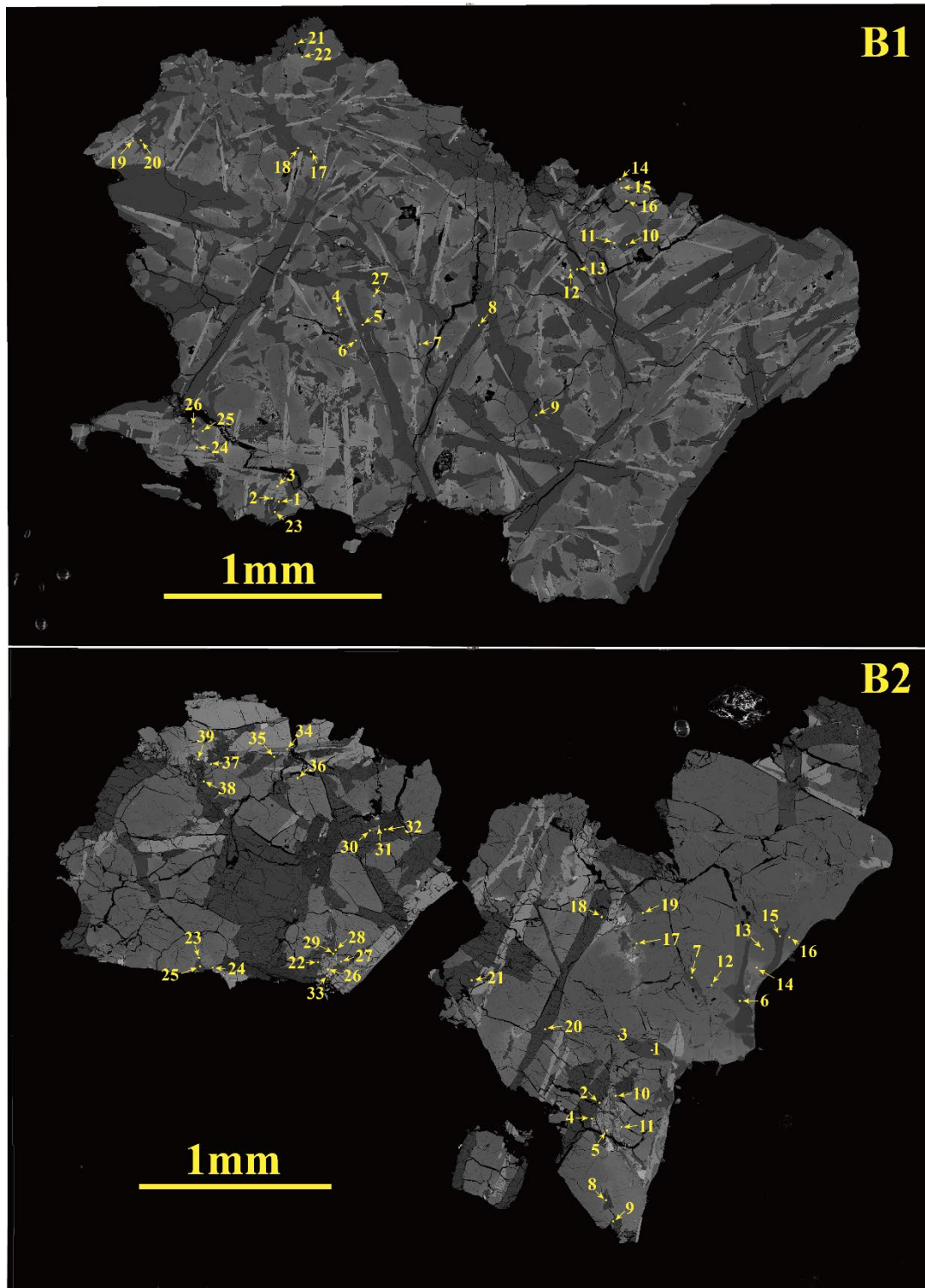
Fig. S9. Locations of Raman analysis of minerals from CE-5-B1 and CE-5-B2. Labels correspond to the numbers presented in the tables (Data S5 and Data S6)
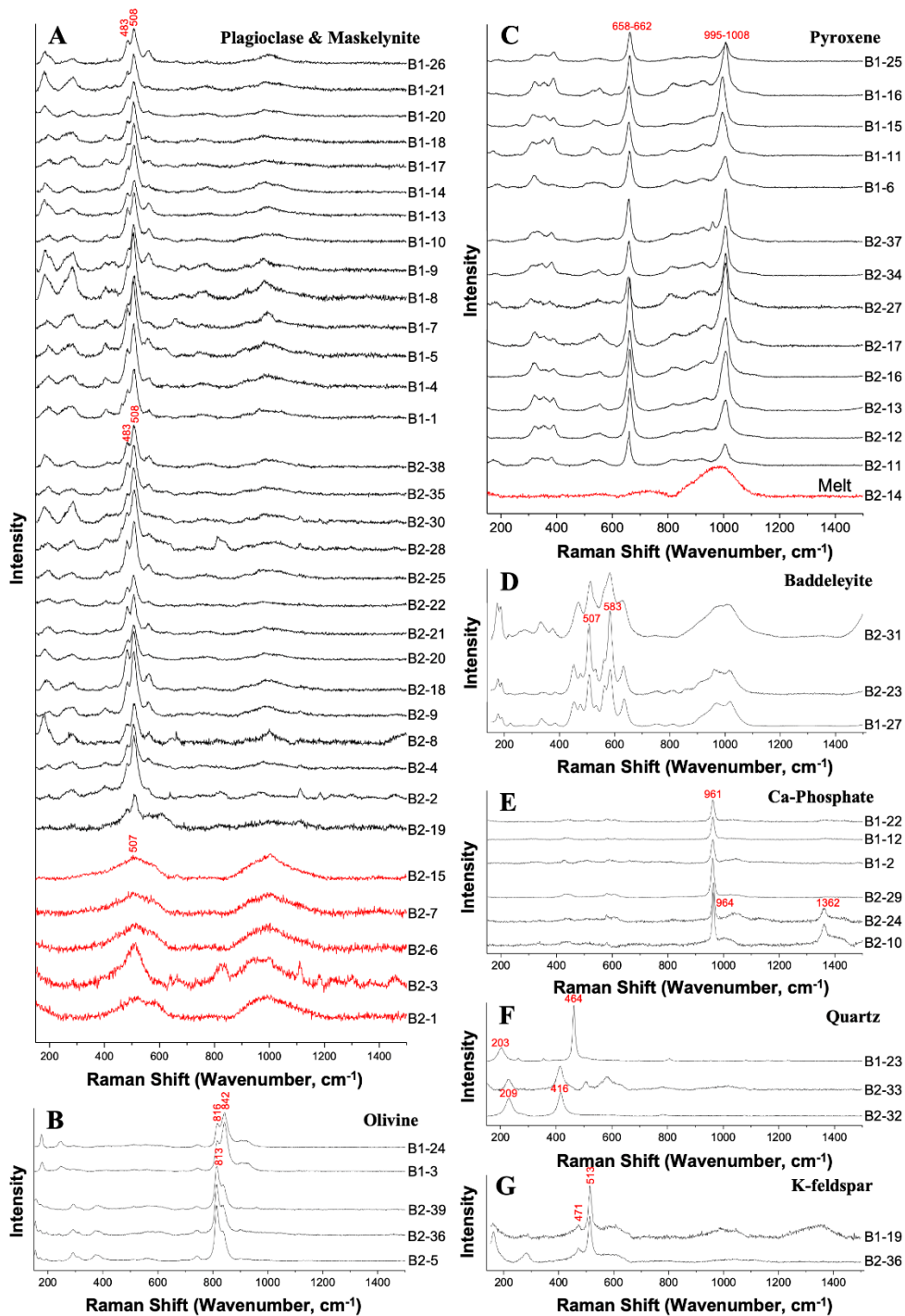
Fig. S10. Results of Raman analysis of minerals from CE-5-B1 and CE-5-B2. Different minerals are shown in different panels. Red curves indicate glass and maskelenyte
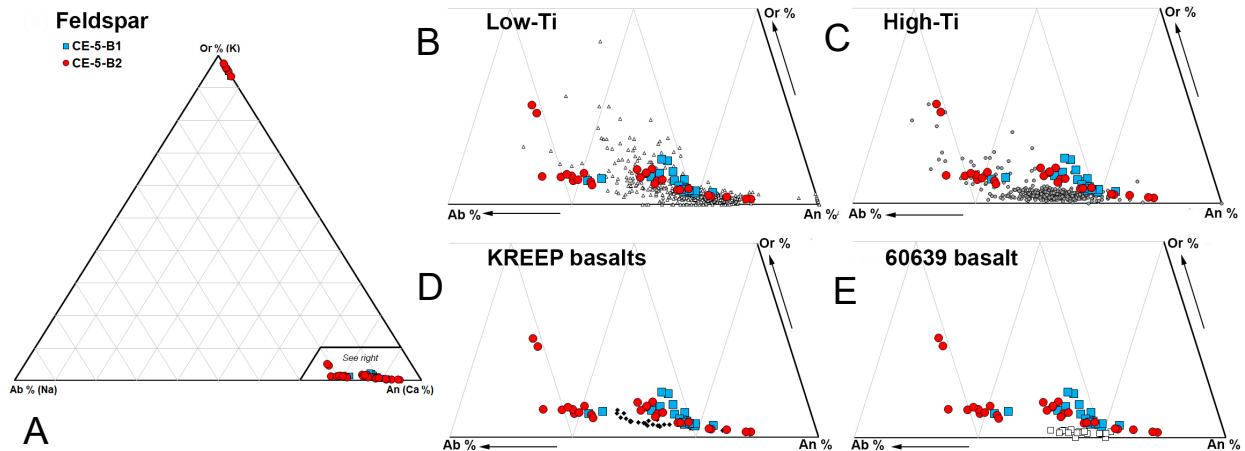
355

Fig. S11. Plagioclase mineral chemistry in basalt fragments CE-5-B1 (blue symbols) and CE-5-B2 (red symbols). (a) Full plagioclase ternary showing range of Ca-rich plagioclase and K-feldspars. Ca-rich plagioclase are compared with (b) Apollo low-Ti mare basalts from the Apollo 12 and 15 landing sites; (c) high-Ti mare basalts from the Apollo 11 and 17 landing sites *(41)*; (d) KREEP basalts *(41, 40)* and (e) intermediate-Ti basalt fragments in sample 60639 *(42)*. All Apollo samples are shown as grey symbols.
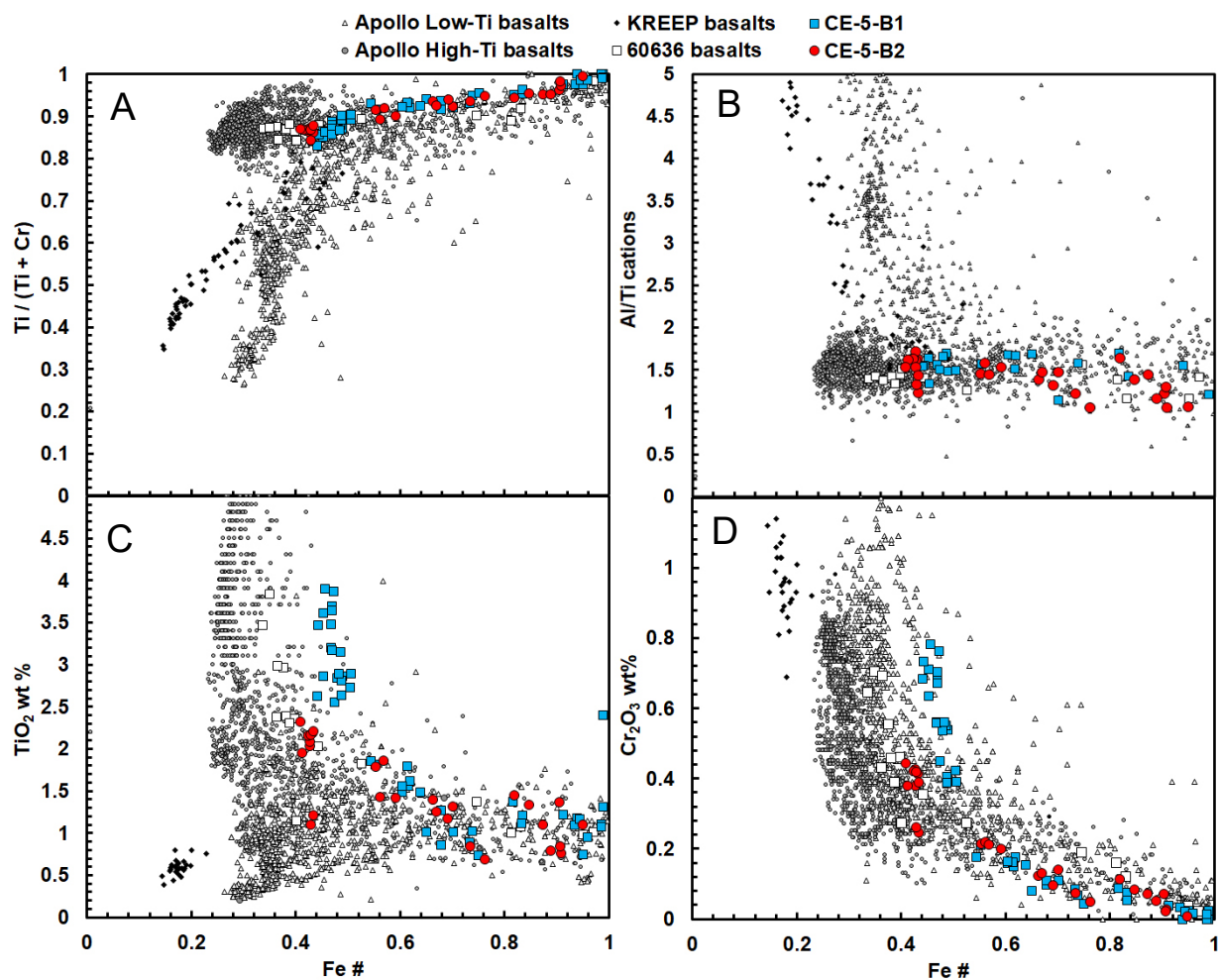
365

370

Fig. S12. Pyroxene minor element composition mineral chemistry in basalt fragments CE-5-B1 (blue symbols) and CE-5-B2 (red symbols). Fe# (Fe/(Fe+Mg)) vs. (a) Ti# (Ti/(Ti+Cr)), (b) Al/Ti (cation ratio), (c) TiO$_2$ wt% and (d) Cr$_2$O$_3$ wt%. Data are compared with Apollo low-Ti mare basalts from the Apollo 12 and 15 landing sites; high-Ti mare basalts from the Apollo 11 and 17 landing sites *(41)*; KREEP basalts *(41, 40)* and intermediate-Ti basalt fragments in sample 60639 *(42)*.
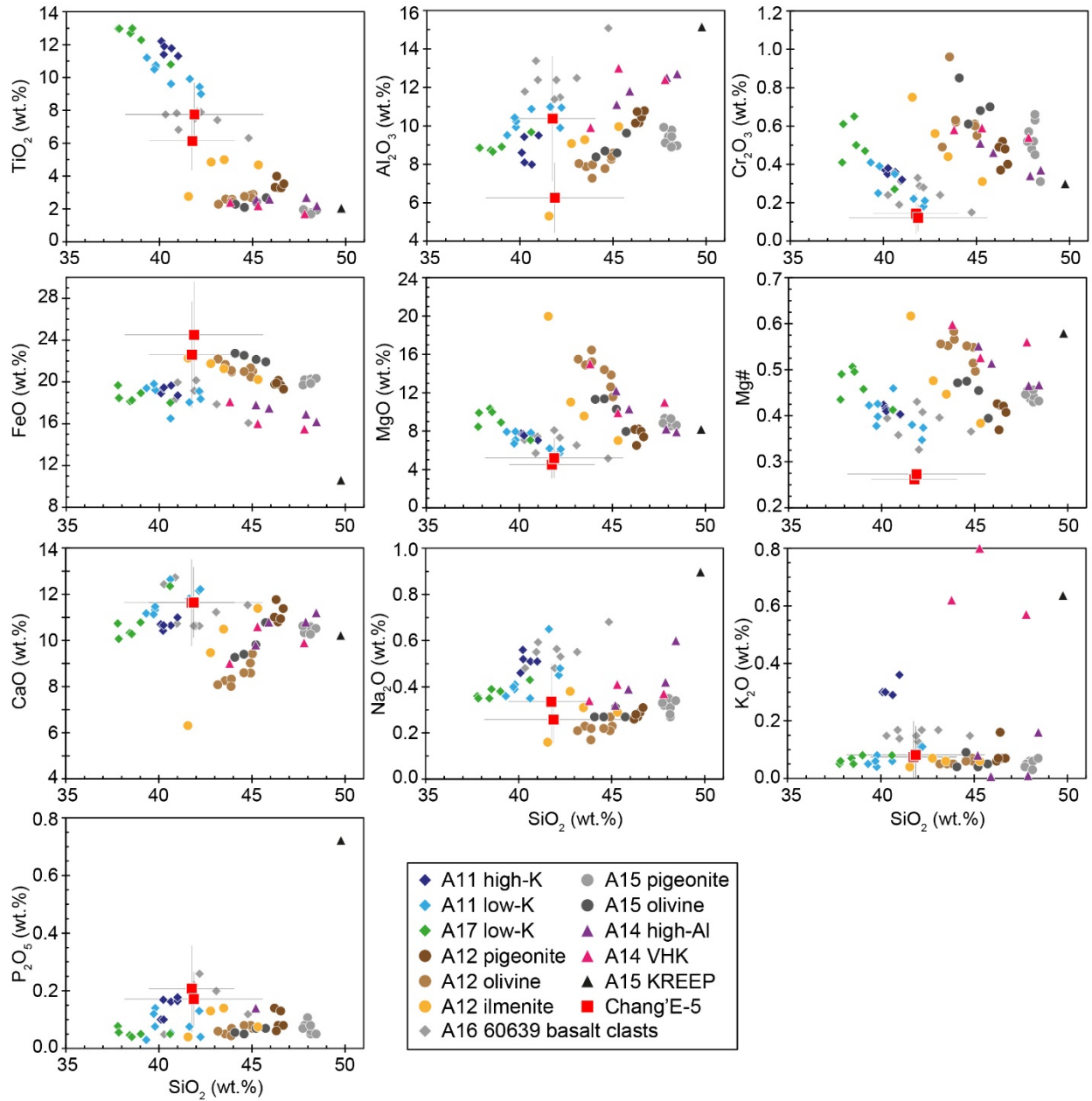
Fig. S13. Whole rock composition estimates for CE5 fragments compared to various types of lunar mare basalts. Literature data are from *(42-44)*. Symbols are the same as Figure 2.

Table S1. Modal and bulk chemical compositions of basalt fragments from Chang'e 5 sample.

Modal compositions	CE5-B1		CE5-B2	
Clinopyroxene (vol.%)	51.244		64.611	
Olivine	4.827		1.882	
Plagioclase	34.371		19.998	
Silica	1.014		2.243	
Ilmenite	6.743		9.286	
Troilite	0.303		0.368	
K-feldspar	0.003		0.099	
K-rich glass	0.562		0.720	
Ca-phosphates	0.457		0.392	
Bulk chemistry	CE5-B1	±1SD	CE5-B2	±1SD
SiO_2 (wt.%)	41.75	2.29	41.87	3.70
TiO_2	6.14	1.77	7.76	1.92
Al_2O_3	10.38	3.23	6.26	1.82
FeO	22.60	5.09	24.50	5.08
MnO	0.29	0.09	0.33	0.08
MgO	4.49	1.42	5.17	2.05
CaO	11.64	1.87	11.65	1.52
Na_2O	0.34	0.17	0.26	0.10
K2O	0.07	0.12	0.08	0.10
Cr_2O_3	0.14	0.11	0.12	0.07
P_2O_5	0.21	0.15	0.17	0.09
Total	98.05		98.17	
Mg#	26.2	10.2	27.3	12.2

390

Data S1. (separate file)
EMP data for minerals and glass in basalt fragments CE5-B1 and CE5-B2

Data S2. (separate file)
EMP data for standards obtained during analysis of basalt fragments CE5-B1 and CE5-B2

395 **Data S3. (separate file)**
Average compositions of minerals in basalt fragments CE5-B1 and CE5-B2

Data S4. (separate file)

Muticollector SHRIMP Pb data obtained for two basalt fragments from Chang'e 5 sample and reference glasses BCR-2G and BHVO-2G.

400

Data S5. (separate file)

Raw Raman data collected for minerals in two basalt fragments

Data S6. (separate file)

405   Raman data for minerals in two basalt fragments corrected for background